8-2011

On the Variation of Gravity Wave Activity through the Solar Cycle at the South Pole

Ryan Matthew Agner
Embry-Riddle Aeronautical University - Daytona Beach

ON THE VARIATION OF GRAVITY WAVE ACTIVITY THROUGH THE SOLAR CYCLE AT THE SOUTH POLE

By

Ryan Matthew Agner

A Thesis Submitted to the

Physical Sciences Department

In Partial Fulfillment of the Requirements for the Degree of

Master of Science in Engineering Physics

Embry-Riddle Aeronautical University

Daytona Beach, Florida

August 2011

ON THE VARIATION OF GRAVITY WAVE ACTIVITY THOUGH THE SOLAR CYCLE AT THE SOUTH POLE

by

RYAN MATTHEW AGNER

This thesis was prepared under the direction of the candidate's Thesis Committee Chair, Dr. Matthew D. Zettergren, Assistant Professor, Daytona Beach Campus, and has been approved by the Thesis Committee. It was submitted to the Department of College of Arts and Sciences in partial fulfillment of the requirements for the degree of Masters of Science in Engineering Physics

Thesis Review Committee:

Matthew D. Zettergren, PhD.
Committee Chair

Michael P. Hickey, PhD.
Committee Member

John M. Hughes, PhD.
Committee Member

MSEP
Graduate Program Chair,
Peter Erdman, PhD.

Physical Sciences
Department Chair,
Michael P. Hickey, PhD.

William F. Grams, PhD.
Dean, College of Arts and Sciences

Robert Oxley, PhD.
Associate Vice President of Academics

9-7-2011
Date

ABSTRACT

Author: Ryan Matthew Agner

Title: On the Variation of Gravity Wave Activity through the Solar Cycle at the South Pole

Institution: Embry-Riddle Aeronautical University

Degree: Master of Science in Engineering Physics

Year: 2011

Atmospheric dynamics comprise of a multitude of phenomena from various sources that affect the entire climate of the globe. Some of these phenomena include Atmospheric Gravity Waves which are ubiquitous features around the planet. They are important mechanisms for the transport of momentum and energy from the lower atmosphere to the upper atmosphere. The sun is the ultimate source of energy for the earth and the primary driver of atmospheric dynamics. The 11-year solar cycle of the sun has had a noticeable effect on the overall climate of the earth in the past. More recent work has seen the diurnal tides being directly influenced by the change in solar energy over the solar cycle at the South Pole. The different types of atmospheric waves interact with each other in complex manners that are still a subject of research today. Gravity waves are known to be modulated by solar tides and vice versa so a change in the tides will induce a change in gravity waves. The solar cycle influence on tides can then be seen overall in gravity wave wavelengths and speeds. A CCD Spectrometer is used to gather temperatures and brightness's of two separate airglow layers in the upper atmosphere at 87km (OH) and 93km (O_2). Two different years are chosen to be analyzed for solar cycle dependencies. One year is 2002, during the previous time of maximum solar activity and the other is 2010, just after the last minimum of solar activity. Time series of temperatures and brightness's are analyzed for gravity

waves activity though a lomb-scargle frequency analysis and a least-squares fit using a sine-cosine wave model. Using gravity waves theory and four different detection methods, the vertical and horizontal wavelengths, phase speeds and group velocities are found for these waves during the 2002 data gathering season and the 2010 data gathering season. Most wave parameters are found to have an overall increase from 2002 to 2010 with the exception being the derived horizontal wavelengths. The calculated wave parameters are found to be in agreement with past gravity wave detections.

ACKNOWLEDGEMENTS

I would first like to thank my wife of 3 years, Nikisha. She is one of the major reasons that I chose to pursue my Master's Degree at this time and has been a constant source of love and support in the entire time I have known her. You are my life, thank You for everything.

I would like to thank Dr. Zettergren for providing the guidance throughout the thesis work and writing. Your ideas and suggestions were invaluable to my effort of this entire project. To my committee members Dr. Hickey and Dr. Hughes, thank you for lending your time and expertise in reviewing this body of work. I look forward to working with you both in the future.

Thank you to Dr. Sivjee and Dr. Azeem for choosing to hire me to work in SPRL. Without this opportunity I would not be where I am today.

Thanks go to my Mother, Carole Rogers and my Father, Samuel Agner Jr. for your unconditional love and support throughout my entire life and for instilling in me your values, morals and ethics that guide me. Thanks also go to my older sister, Amanda and my younger sister, Sarah. We have all been through good times and bad times and have emerged from them with stronger bonds than before. To my mother-in-law and sister-in-law I would like to express my gratitude for everything you have given both of us, from coming all the way from India for our wedding and for your love from half-way across the world. Thanks are given to my entire family for everything you have given me throughout my life.

TABLE OF CONTENTS

LIST OF FIGURES

LIST OF TABLES

CHAPTER 1 - INTRODUCTION

Atmospheric waves play an important role in climate throughout the entire atmosphere by transporting momentum and energy around the globe which has a profound effect on our daily weather patterns. There are three main types of large scale atmospheric waves and each of them has their own properties that affect the atmosphere in different ways. The longest of these waves are planetary waves, which are caused by the shear on the atmosphere from the change in the Coriolis force with latitude and typically have periods on the order of days and wavelengths thousands of kilometers long. The second type is atmospheric tides which are caused by the periodic heating of the atmosphere by the sun as the earth rotates. Since these are due to the earth's rotation the main atmospheric tide has a period of one day with other tides at a few harmonics below this. The last type, which this thesis will focus on, is Atmospheric Gravity Waves. Gravity Waves have far more variability in their properties than planetary waves and tides because of their greater amount of sources.

Ultimately, all atmospheric wave activity is driven by the energy flux from the sun incident onto the atmosphere. This influx of energy has a noticeable 11 year pattern in magnitude as the sun itself goes through an 11 year solar cycle. The effect of the solar cycle on gravity waves has not been a topic of any major research. Most solar cycle dependence studies have been on the atmospheric tides because of their source being the influx of solar energy. The diurnal (24 hour) tide in the Antarctic for example, was shown to have dependence in its intensity upon this solar cycle [Azeem and Sivjee, 2009]. Gravity wave sources on the other hand are far more varied such as air flow over a mountain range, disturbances from a thunderstorm or some small perturbation in a jet stream or wind. While these sources tend to be in the troposphere or stratosphere, gravity waves travel upward and encounter other gravity

waves, tides or planetary waves already present in the upper atmosphere which can change some of their properties. Specifically, gravity waves can be modulated by the 12 and 24 hour tides over the Antarctic [Beldon and Mitchell, 2010].

The previous solar cycle lasted from 1996 till 2008, the time from a minimum of solar activity to the next, with a peak of activity in 2002. The minimum at the end of this cycle proved to be unusual due to both its long length and the depth that it reached. This extended minimum is an ideal period of time to study solar cycle influence on wave activity since the sun provides the source of energy for atmospheric tides which in turn can modulate gravity waves. With the influx of solar energy decreased and the tides that modulate gravity waves undergoing changes in intensity, gravity waves that propagate throughout the atmosphere should also go through a similar change in activity.

1.1 GOALS

This thesis will provide insight into one component of the complex dynamics and wave-wave interactions of the upper atmosphere and the solar cycle influences on them by analyzing how the average gravity wave parameters change from solar maximum to solar minimum. It will present data that has not been explored before in previous gravity wave seasonal and inter-annual studies. The work presented here will also provide an analysis method for gravity wave detection to be used by students working at the Embry-Riddle Space Physics Research Lab.

1.2 THESIS OUTLINE

Chapter 2 of this thesis will begin with background information about basic gravity wave theory and will continue on to a review of previous research related to this analysis. Chapter 3 will explain the instrument used to collect the data and the method used to derive gravity wave

parameters from a time series of brightness' and temperatures for the OH and O_2 airglow layers. Chapter 4 will contain the results and analysis section detailing the various vertical and horizontal gravity wave parameters found and the differences between the South Pole 2002 data gathering season and the South Pole 2010 data gathering season which are from April till September. Chapter 5 will give a final conclusion to the work and directions for future research on this subject.

CHAPTER 2 - BACKGROUND

2.1 THE SOLAR CYCLE

The influx of energy from the sun is the main source of life for the planet and a driver of planetary atmospheric dynamics. The amount of energy that is irradiated onto the earth is called the solar constant and has a value of $1{,}360\,\frac{W}{m^2}$. This term is slightly misleading though, because the solar constant is not actually constant and has variations from two main sources. The first is a yearly variation simply due to the changing distance between the earth and sun from the earth's slightly eccentric orbit. This only causes a change of a few percent throughout the year and is not thought to affect the earth's climate in any appreciable way. The other major energy variation is from what is called the solar cycle which is an 11 year cycle that the sun goes through in solar activity.

There are two main ways of observing this cycle from the earth, one by counting the number of sunspots that appear on the sun's surface and another by monitoring the flux at a radio wavelength of 10.7cm. Sunspots are dark spots on the surface of the sun and are caused by magnetic field lines coming up through the surface of the sun and decreasing the convection in that area. This causes it to be cooler than the rest of the surface of the sun which is why they appear as dark spots. The sunspot numbers provide an indirect way of measuring the solar activity since the amount of solar field lines emerging from the surface of the sin will decrease with decreased activity, hence less sunspots. The flux at the 10.7cm radio wavelength (F10.7 flux) is a measure of the amount of energy at that particular wavelength which is a direct measure of the amount of solar flux at the earth. This has been an important and useful measurement of the solar activity since records of it began being recorded in 1947. From Figure 2-1 the sunspot number and the F10.7 flux match very well with each other. The 11 year cycle

from solar maximum to solar minimum is also clearly seen with the peaks corresponding to solar maximum and the valleys corresponding to solar minimums.

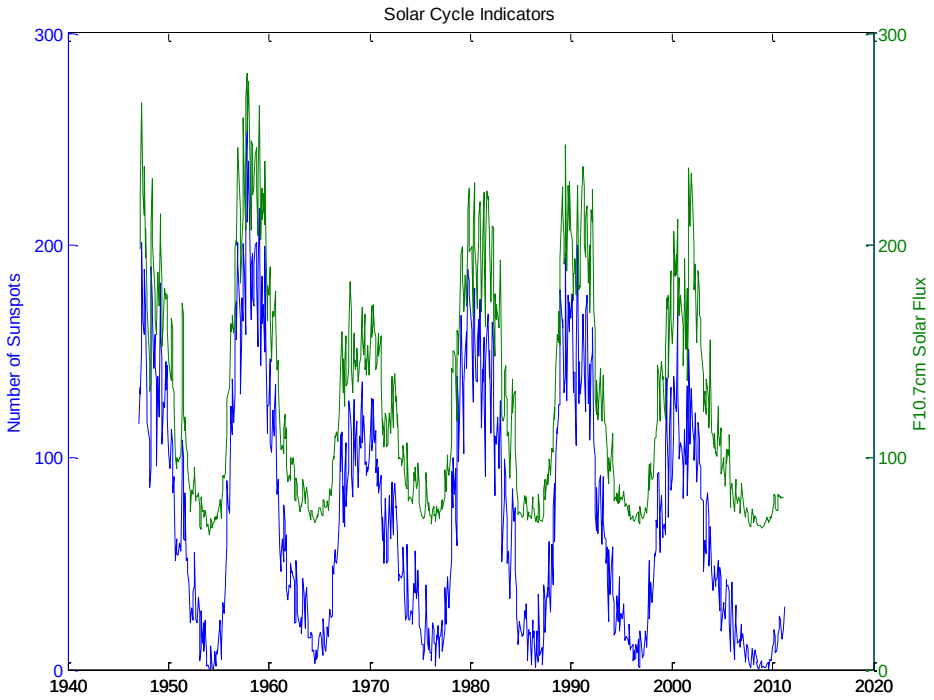

Figure 2-1: Number of sunspots and f10.7cm solar flux from 1947 to 2011

This cycle has had a large effect on the climate of the planet in the past, most clearly in a period known as the Maunder Minimum. This was a time between 1645 and 1715 in which there were very few sunspots observed on the sun [Eddy, 1976]. The Little Ice Age, which was a decrease in global temperatures over an extended period of time from the late 1600's and into the early 1700's, is believed to have been significantly influenced by the Maunder Minimum. This type of clear effect on ground temperatures is not easily seen in modern times due the increased amount of greenhouse gasses in the atmosphere since the industrial revolution. Figure 2-2 shows how the global mean temperature has actually been increasing steadily since 1900 without showing the same cyclical variation as seen in the incident solar flux.

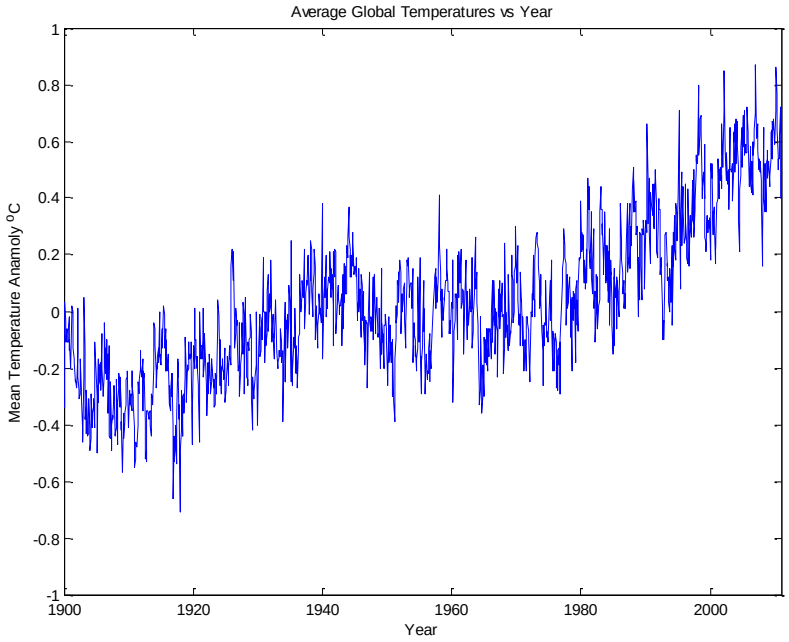

Figure 2-2: Global Surface Mean Temperature Anomaly from 1900 to 2011

This can causes the total energy in the atmosphere to decrease which will change the dynamics such as winds and wave activity.

2.2 GRAVITY WAVE THEORY

Gravity waves are small scale ubiquitous features in the atmosphere that have large scale influences on atmospheric dynamics. They are buoyancy waves which are generated through various means in the lower and middle atmosphere. As a parcel of air is lifted through some sort of disturbance it will encounter air that is less dense than itself. This parcel of air will then be heavier than the surroundings so gravity will force it back down overshooting its equilibrium position. The parcel will then be denser than its surroundings so a buoyant force will push it back up, overshooting it equilibrium position again. This causes oscillations as the buoyant force and gravity work against each other on the air parcel. Some sources of gravity waves include air flow over a mountain, atmospheric disturbances from storm systems, or from geostrophic adjustment

[Meriwether, 2007]. Figure 2-3 shows how gravity waves propagate along slanted paths giving both horizontal and vertical components to them. These components can be measured by their influence on airglow intensities, atmospheric temperatures and density.

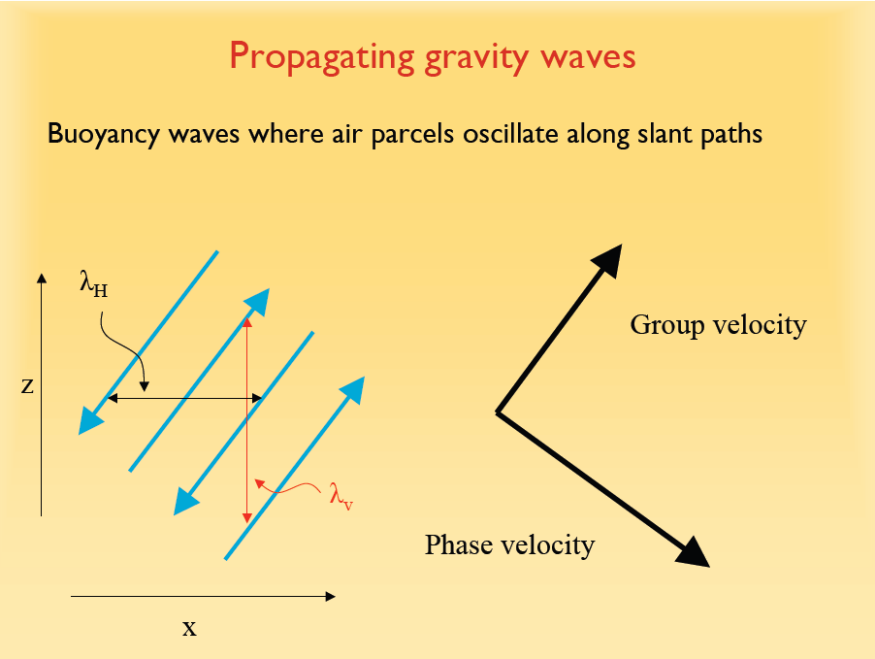

Figure 2-3: Pictorial Representation of Gravity Wave Propagation [Meriwether, 2007]

2.2.1 DERIVATION OF THE GRAVITY WAVE DISPERSION RELATION

The gravity wave dispersion relation is a mathematical expression which relates the angular frequency of a gravity wave with its vertical and horizontal wavenumbers. Much of the work on gravity wave theory and mathematical descriptions was established by Hines [1960]. Hines assumed a stationary atmosphere without any temperature or composition variations. The gravitational field is also taken to be constant throughout the wave propagation region. First the Euler equations of conservation of mass, conservation of momentum and the conservation of energy [Shunk, 1977] are used and subjected to small perturbations.

$$\frac{\partial \rho}{\partial t} + \nabla \cdot (\rho \vec{u}) = 0 \qquad \text{Equation 1}$$

$$\rho\left(\frac{\partial \vec{u}}{\partial t} + \vec{u} \cdot \nabla \vec{u}\right) = \rho \vec{g} - \nabla p \qquad \text{Equation 2}$$

$$\frac{\partial p}{\partial t} + \vec{u} \cdot \nabla p = -\frac{5}{3} p \nabla \cdot \vec{u} \qquad \text{Equation 3}$$

Small perturbations in pressure, density and velocity with the non-perturbed values being set to constants are shown with the following set of equations.

$$\rho = \rho_0 + \rho_1, \quad p = p_0 + p_1, \quad \vec{u} = \vec{u}_0 + \vec{u}_1, \qquad \text{Equation 4}$$

$$\frac{\partial \rho_0}{\partial t} = 0, \quad \frac{\partial p_0}{\partial t} = 0, \quad \frac{\partial \vec{u}_0}{\partial t} = 0. \qquad \text{Equation 5}$$

Where, ρ_0, p_0, and $\vec{u}_0$ are the non-perturbed neutral density, atmospheric pressure and wind velocity vector respectively and ρ_1, p_1, and $\vec{u}_1$ are the small perturbations in each. Replacing the density and wind in Equation 1 with the perturbations from Equation 4 gives the following

$$\frac{\partial \rho_1}{\partial t} + \nabla \cdot [(\rho_0 + \rho_1)(\vec{u}_0 + \vec{u}_1)] = 0, \qquad \text{Equation 6}$$

$$\frac{\partial \rho_1}{\partial t} + \nabla \cdot [\rho_0 \vec{u}_0 + \rho_0 \vec{u}_1 + \rho_1 \vec{u}_0 + \rho_1 \vec{u}_1] = 0. \qquad \text{Equation 7}$$

Taking the background wind, $\vec{u}_0$, to be zero and neglecting any second order terms or higher in order to linearize the equation, Equation 7 becomes

$$\frac{\partial \rho_1}{\partial t} + \nabla \cdot (\rho_0 \vec{u}_1) = 0, \qquad \text{Equation 8}$$

$$\frac{\partial \rho_1}{\partial t} + \nabla \rho_0 \cdot \vec{u}_1 + \rho_0 \nabla \cdot \vec{u}_1 = 0. \qquad \text{Equation 9}$$

Which is the Equation of Continuous Mass Conservation from Hines [1960].

Taking Equation 2 and inserting the perturbed values from Equation 6 yields

$$(\rho_0 + \rho_1)\left(\frac{\partial \vec{u}_1}{\partial t} + \vec{u}_1 \cdot \nabla \vec{u}_1\right) = \rho \vec{g} - \nabla p_0 - \nabla p_1. \qquad \text{Equation 10}$$

With the second order terms and higher and the $\vec{u}_1 \cdot \nabla \vec{u}_1$ term assumed to be very small the equation reduces to

$$\rho_0 \frac{\partial \vec{u}_1}{\partial t} = \rho_0 \vec{g} - \nabla p_0 - \nabla p_1 + \rho_1 \vec{g}. \qquad \text{Equation 11}$$

Since $\nabla p_0 = \rho_0 \vec{g}$ this reduces into the Linearized Equation of Motion from Hines [1960].

$$\rho_0 \frac{\partial \vec{u}_1}{\partial t} = \rho_1 \vec{g} - \nabla p_1 \qquad \text{Equation 12}$$

Now taking Equation 3 and inserting the perturbed values of pressure and wind velocity, the equation becomes

$$\frac{\partial p_1}{\partial t} + (\vec{u}_0 + \vec{u}_1) \cdot \nabla (p_0 + p_1) = -\frac{5}{3}(p_0 + p_1) \nabla \cdot \vec{u}. \qquad \text{Equation 13}$$

Neglecting higher order terms and replacing 5/3 with γ, the ratio of specific heats, Equation 13 becomes

$$\frac{\partial p_1}{\partial t} + \vec{u}_1 \cdot \nabla p_1 = -\gamma p_0 \nabla \cdot \vec{u}. \qquad \text{Equation 14}$$

Now solving Equation 9 for $\nabla \cdot \vec{u}$ as shown in the following equation

$$\nabla \cdot \vec{u} = -\frac{1}{\rho_0}\left(\frac{\partial \rho_1}{\partial t} + \nabla \rho_0 \cdot \vec{u}_1\right), \qquad \text{Equation 15}$$

and inserting it into Equation 14 so that it becomes

$$\frac{\partial p_1}{\partial t} + \vec{u}_1 \cdot \nabla p_1 = \frac{\gamma p_0}{\rho_0}\left(\frac{\partial \rho_1}{\partial t} + \nabla \rho_0 \cdot \vec{u}_1\right). \qquad \text{Equation 16}$$

The first term on the right hand side is equal to the square of the speed of sound c as follows

$$\frac{\gamma p_0}{\rho_0} = c^2. \qquad \text{Equation 17}$$

With this replaced, Equation 16 then becomes the Equation of Adiabatic State from Hines [1960].

$$\frac{\partial \rho_1}{\partial t} + \vec{u}_1 \cdot \nabla p_1 = c^2 \left(\frac{\partial \rho_1}{\partial t} + \nabla \rho_0 \cdot \vec{u}_1 \right) \quad \text{Equation 18}$$

The Linearized Equation of Motion, the Equation of Adiabatic State and the Equation of Continuous Mass Conservation are the three equations that describe atmospheric oscillations. A plane wave solution for the atmospheric oscillation equations above can be found as:

$$U(x, z, t) = Ae^{i(\omega t - Kx - Mz)} \quad \text{Equation 19}$$

Where K is the horizontal wavenumber, M is the vertical wavenumber, A is the wave amplitude and ω is the observed wave frequency. The wavenumbers in the above wave equation can be shown to be related to each other by the following dispersion relation [Hines, 1960]:

$$\omega^4 - \omega^2 c^2 (K^2 + M^2) + (\gamma - 1) g^2 K^2 + i\gamma g \omega^2 M = 0 \quad \text{Equation 20}$$

Due to the terms with gravitational acceleration, this relation does not give any solution where both *K* and *M* are purely real and nonzero. To solve this relation the horizontal wavenumber has to be considered to be only real, *K*=*k*. The vertical wavenumber can then be either complex, real or purely imaginary. A purely imaginary vertical wavenumber indicates no vertical propagation which is an evanescent wave. A complex vertical wavenumber indicates a wave that propagates upward through the atmosphere and is what this paper concerns. The complex vertical wavenumber takes the form of

$$M = m + \frac{i}{2H}, \quad \text{Equation 21}$$

where $H = \frac{c^2}{\gamma g}$ is the scale height of the atmosphere. Substituting the purely real horizontal wavenumber and the complex vertical wavenumber into the dispersion relation, it becomes:

$$\omega^4 - \omega^2 c^2(k^2 + m^2) + (\gamma - 1)g^2k^2 - \frac{\gamma^2 g^2 \omega^2}{4c^2} = 0. \quad \text{Equation 22}$$

From this relation, any pair of real wavenumbers are associated with only one value of ω^2 and hence two values of ω. greater than $\omega_a = \frac{\gamma g}{2c}$, the acoustic cutoff frequency, and less than $N = \frac{\sqrt{\gamma - 1}g}{c}$, the Brunt-Vaisala Frequency. Using these frequencies, the dispersion relation can be written as

$$\frac{(\omega^2 - \omega_a^2)\omega^2}{c^2} - \omega^2(k^2 + m^2) + N^2k^2 = 0. \quad \text{Equation 23}$$

This dispersion relation can then be solved for the vertical wavenumber and put in the more common form from Hickey and Yu [2005]

$$m^2 = \frac{(N^2 - \omega^2)}{\omega^2}k^2 - \frac{(\omega^2 - \omega_a^2)}{c^2}. \quad \text{Equation 24}$$

This derivation assumes that the atmosphere is motionless and irrotational, i.e. no background wind. The observed frequency, ω, in this case will then be equal to the frequency of the wave relative to the fluid medium, the intrinsic frequency Ω. If there is a constant background horizontal wind present then the observed wave frequency as seen on the ground is Doppler shifted based upon the horizontal wind speed, $\vec{u}_0$. The intrinsic frequency will then be

$$\Omega = \omega - \vec{k}\vec{u}_0. \quad \text{Equation 25}$$

The dispersion relation for an atmospheric gravity wave with a constant background wind is found by replacing ω in Equation 24 with the intrinsic frequency from Equation 25 as follows [Hines, 1960]

$$m^2 = \frac{(N^2 - \Omega^2)}{\Omega^2}k^2 - \frac{(\Omega^2 - \omega_a^2)}{c^2}. \quad \text{Equation 26}$$

The Brunt-Vaisala frequency, *N*, and the acoustic cutoff frequency, ω_a, can both be solved if the speed of sound, *c*, in the medium is known, which can be found using Equation 17, if the unperturbed density and pressure of the atmosphere are known. As will be seen in Chapter 3, the gravity wave detection method used here can only directly detect vertical properties of any atmospheric gravity wave passing through an airglow layer. The dispersion relation with a constant background wind, Equation 26, will be used to infer the horizontal wave number of any detected atmospheric gravity wave.

2.2.2 THE KRASSOVSKY RATIO

Observations of gravity waves have been performed for many years using all sky cameras and spectrometers in the hydroxyl airglow layer. Krassovsky [1972] introduced the ratio

$$\eta = \frac{\delta I / \bar{I}}{\delta T / \bar{T}}, \qquad \text{Equation 27}$$

known as the Krassovsky ratio, where δI is the intensity perturbation of the airglow layer due to a passing gravity wave, $\bar{I}$ is the time averaged intensity, δT is the temperature perturbation of the airglow layer due to the passing gravity wave and $\bar{T}$ is the time averaged temperature. This ratio is a numerical value that relates the relative strength of the intensity variations to the strength of the temperature variations in a gravity wave. It was used for many years to help characterize different gravity waves and to compare them to each other as well as to compare the validity of gravity wave models with airglow data. A phase difference between the intensity oscillations and the temperature oscillations can be seen by writing the ratio in phasor notation

$$\eta = \frac{A_I e^{i\Phi_I}}{A_T e^{i\Phi_T}} = \frac{A_I}{A_T} e^{i(\Phi_I - \Phi_T)}, \qquad \text{Equation 28}$$

where A_I is the amplitude of the intensity oscillation, A_T is the amplitude of the temperature oscillation, Φ_I is the phase of the intensity or brightness oscillation and Φ_T is the phase of the temperature oscillation. The phase difference is then

$$\Phi = \Phi_B - \Phi_T. \qquad \text{Equation 29}$$

The phase of the Krassovsky ratio is positive if the brightness oscillation leads the temperature oscillation [Reisin and Scheer, 1996]. From the chemistry involved in the airglow layers, a positive phase (brightness leads) means that the energy of the wave is propagating downward with upward phase progression. This is due to the slight altitude difference between the peak perturbation of the brightness emission and the peak perturbation altitude of the temperature.

The Krassovsky ratio makes it possible to determine vertical propagation information of an atmospheric gravity wave using only the intensity perturbation and the temperature perturbation of a single airglow layer as shown by Resin and Sheer in two separate papers [1996 and 2001]. The 1996 paper focused on the comparison of waves in the tidal period range (3-24 hours) separately in both the OH and O_2 atmospheric airglow layers at mid-latitudes from two separate stations. One station was located at 37^{o}N at El Arenosillo, Spain and the other at 32^{o}S in El Leoncito, Argentina. They were able to use the two equations from Tarasick and Hines [1990] to derive vertical wavelengths of these long period waves in each layer separately by using the derived temperatures and intensities by the following relation

$$\lambda_z = \frac{2\pi\gamma H}{(\gamma - 1)|\eta| \sin \Phi}. \qquad \text{Equation 30}$$

where γ is the ratio of specific heats, H is the atmospheric scale height, η is the krassovsky ratio and Φ is the phase angle of the Krassovsky ratio. They then compared the values of these wavelengths and of the complex Krassovsky ratio to past results [Hecht & Walterscheid, 1991;

Zhang et al., 1993a, Hecht at al., 1987, Sivjee et al., 1987, Swenson et al., 1990, and Oznovich et al., 1995] and found the results for each layer in agreement with these experimentally derived ratios and the Tarasick and Hines relations for waves in the tidal range.

2.3 LITERATURE REVIEW

The importance of gravity waves energy transport and their effect on the atmosphere was not always well understood. One of the biggest questions in atmospheric research in the middle part of the century was what exactly was causing the summer mesopause temperature at high latitudes to be cooler than the winter mesopause temperatures. While it was known that some sort of atmospheric friction was the cause, the cause of this friction was not known. This question was answered by Lindzen [1981] using a WKB method coupled with experimental rocket data to derive acceleration of the mean zonal flow due to gravity wave breakdown. This result showed that gravity waves were not just some noise on top of the tidal waves but were in themselves a significant driver of upper atmospheric dynamics.

The work of Hines and Tarasick [1987 and 1990], has been used as a basis for gravity wave observational research by developing mathematical relations for the effects of gravity wave passage through a single airglow layer. They make it possible to determine the vertical wave characteristics of a wave using only the measured brightness and temperature variations. These relations take into account off zenith observations which are necessary because the measured brightness of an airglow layer is not from a single thin layer but vertically integrated through several kilometers. An off zenith observation would actually be looking through more of the airglow layer compared to a zenith one which would affect the detected brightness and temperature.

The Hydroxyl (OH) Meinel airglow has been a very useful atmospheric layer to observe when looking for gravity wave signatures. Hydroxyl is a very reactive molecular agent due to having only one valence electron. This causes it to have the possibility to combine with a multitude of species such as ozone (O_3) and hydroperoxyl (HO_2). As a result of these reactions the hydroxyl will release photons at specific wavelengths that can be seen from the ground. The high number of reactions as well as the concentrations of the OH at 87km altitude causes it to have a high intensity in the nighttime airglow. As a gravity wave moves through this region the airglow layer will be perturbed by a measurable amount that can be seen with several types of instruments such as all-sky imagers as seen in Figure 2-4, or spectrometers [Azeem, Sivjee, 2009; Reisin, Scheer, 2001; Sikha et al. 2010; Yee, Niciejewski and Luo, 1991].

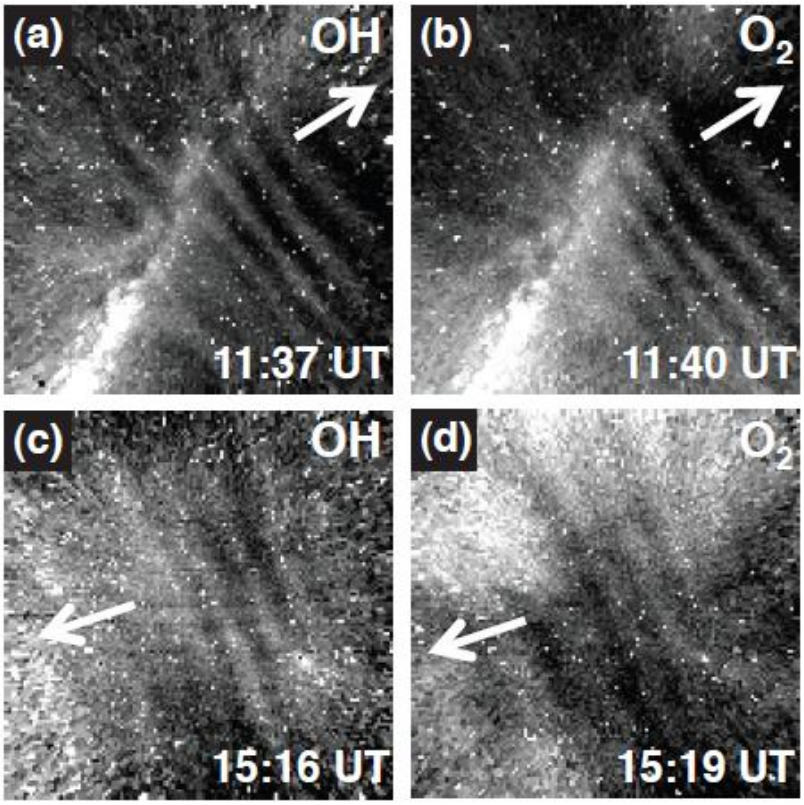

Figure 2-4: Gravity Wave signatures in the OH and O2 Airglow from an all-sky imager [Simkhada et al, 2009]

The O_2 nightglow has not been used as extensively as the OH nightglow in the past. The spectrum of the O_2 atmospheric band has many spectral lines that only have a few Å of separation which make it very difficult to derive temperatures from it unless a model of the quantum mechanics of the molecular bond is developed. The sources and sinks for the O_2 atmospheric band were also not as well understood in the past due to the more complex chemistries involved. Similar to the OH nightglow, the O_2 nightglow will be perturbed in a measurable way by a passing gravity wave. These perturbations can be seen from the same instruments as what is used to detect the OH, just set to a different wavelength range. Hickey, Schubert and Waltersheid [1993] have successfully modeled how the O_2 airglow reacts to a passing gravity wave. This model includes 10 reactions involved in the production of the O_2 atmospheric band including the intermediate creation of the Hertzberg band. Using the fact that the airglow layer is not thin but extends over several kilometers they found that their model fits well with observations of the perturbations in this layer.

Modeling of the gravity influence on both the OH and O_2 layers was conducted by Liu and Swenson [2003]. Their model proved theoretically that the vertical wavelength and damping rate of a gravity wave can be determined from simultaneous observations of both the OH and O_2 airglow layers. A cancellation effect was also taken into account in this analysis to account for the thickness of each airglow layer. As an airglow detection instrument looks up from the ground into the sky, the intensity it sees is the integrated intensity of the entire layer. A wave that travels through the thick layer will induce some fluctuations in brightness. If the wavelength of the wave is too small then it will have more than one vertical wavelength inside the layer itself. This will cause the amplitudes of the wave's airglow brightness and temperature weighted brightness to average out to some degree which means that the observed amplitude will be much smaller than the actual amplitude of the wave. This makes it very difficult to see a wave with a short

wavelength because the cancellation effects inside each airglow layer are so strong that the amplitude of the wave will not be above the background noise as seen from the ground.

Much of the research on variations of gravity waves has been conducted on a seasonal basis such as the work by Rauthe, Gerding, and Lubken [2008]. This was done using a LIDAR instrument at the Leibniz-Institute of Atmospheric Physics in Kuhlungsborn, Germany. This data set was taken sporadically over a time frame from 2002 till 2006 and includes measurement between 1 and 105 kilometers in altitude. By using a LIDAR instrument the propagation of small scale gravity waves can be followed as they travel upward through the stratosphere and mesosphere. From this data set no seasonal dependence on the amount of gravity waves or their wavelengths were found. In this case the mean vertical wavelength was found to be about 20 kilometers so it is shorter than what can be found accurately by using airglow measurements [Hickey and Walterscheid, 1999]. In contrast to this, the amplitude growth of the waves as they travel upwards was found to be stronger in the summer between 70 and 90 kilometer altitudes whereas the amplitude growth is stronger in the winter between 35 and 70 kilometers.

Using the OH airglow layer the tidal variations throughout the solar cycle at the South Pole were derived by Azeem and Sivjee [2009]. Using a Michelson Interferometer at the South Pole research station, the temperatures for the airglow layer at 87km were derived using the method from Sivjee and Hamwey [1987]. This instrument records spectra between 10,000 Å and 17,000 Å and was used to derive the temperatures and brightness' of the OH (3,1) and OH (4,3) Meinel bands. The data set that was used was from 1994 till 2007 and was taken continuously during each polar winter, which lasts from April until September. From this study the diurnal (24 hour) tide showed a strong intensification during the 2001 and 2002 seasons which

correspond to the last solar maximum. In contrast the semi-diurnal (12 hour) tides did not show any clear intensification with the increase in solar output.

CHAPTER 3 - DATA ACQUISITION AND ANALYSIS

3.1 INSTRUMENT DESCRIPTION

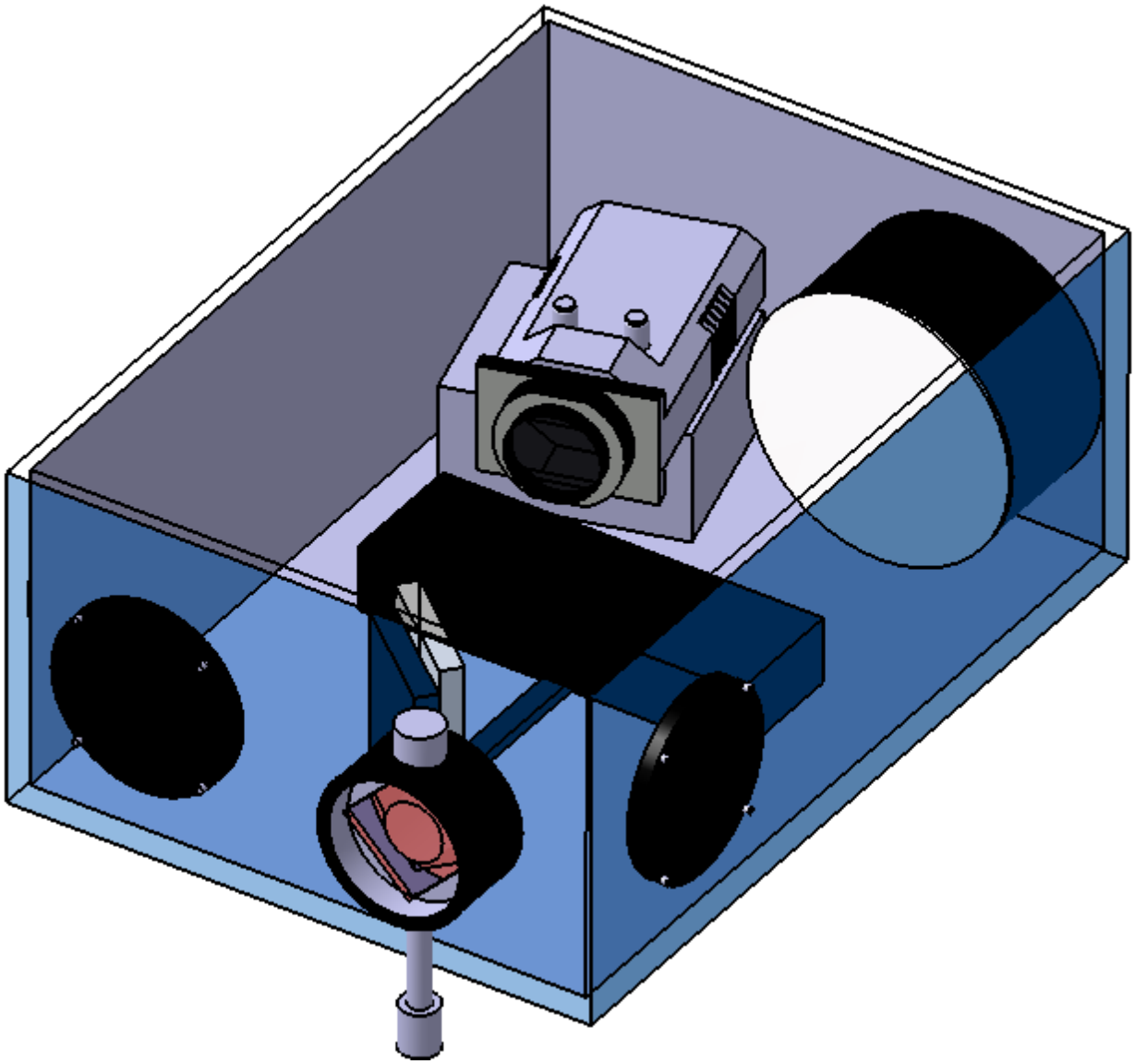

Figure 3-1: Diagram of CCD Spectrometer [Mutiso, 2008]

The instrument used for acquiring the data for both of the selected seasons was a modified Czerny-Turner grating spectrometer with a CCD (Charge Couple Device) scientific camera (Figure 3-1). Light from the night sky enters the aperture at the front of the instrument

and travels through a curved slit with an arc length of 45mm. This light is then reflected off of a spherical mirror with a focal length of 0.5m onto a diffraction grating. A diffraction grating is a rectangular piece of optical equipment which splits the incoming light into different directions depending on its wavelength. It does this due to the grooves that are etched into its surface. As the light hits the grating it will be reflected with each groove acting as a line source for the reflected light. When the light from each of these sources crosses through each other, constructive or destructive interference will occur depending on both the angle of reflection and the wavelength of the light. Most of the light along a single angle will encounter destructive interference except that of a specific wavelength governed by the following equation

$$d * (\sin\theta_m + \sin\theta_i) = m * \lambda, \qquad \text{Equation 31}$$

where d is the groove spacing, λ is the wavelength, θ_m is the angle of the maxima of the reflection, θ_i is the incident angle and m is the order number of the fringe.

The grating used in this instrument is 110mm by 110mm with 1200grooves/mm. After the light is reflected from the grating and split up by wavelength it is sent into an f/1.4, 85mm focal length camera lens attached to the CCD camera.

Between the 2002 South Pole data gathering season and the 2010 season, the instrument used to gather the airglow spectra was changed. All of the components had the same specifications except for the CCD camera. The camera used in 2002 was a Pixelvision camera with a chip size of 1100x330 pixels. The camera used in the 2010 season was an Andor camera with a smaller chip size of 1024x24 pixels. Both were thermoelectrically cooled to -110^{o}C for noise reduction.

The instrument is housed at Amundsen-Scott South Pole research station and is pointed off-zenith (vertical) by 25^{o} and toward the geomagnetic South Pole. Assuming the OH airglow

layer is located at an altitude of 87km, the horizontal position of the observation is 40.6km away from the instrument with the O_2 airglow layer 2.8km farther.

3.2 OH(6-2) CHEMISTRY

The process for the creation and emission for the hydroxyl Meinel band is as follows [Sivjee and Hamwey, 1987].

$$H + O_3 \rightarrow OH(X^2\Pi)(v' \leq 9) + O_2 \qquad \text{Equation 32}$$

$$HO_2 + O \rightarrow OH(X^2\Pi)(v' \leq 6) + O_2 \qquad \text{Equation 33}$$

$$OH(X^2\Pi)(v') \rightarrow OH(X^2\Pi)(v'') + \hbar v \qquad \text{Equation 34}$$

where *H* is hydrogen, O_3 is ozone, *OH* is hydroxyl, O_2 is molecular oxygen, HO_2 is perhydroxyl, and $\hbar v$ is a photon. Within the parentheses, v' is the original vibrational level and v'' is the final vibrational level. The *X* designates the ground state for the molecule, the superscript 2 gives an S quantum number of ½ and the Π describes the type of molecular bond in the molecule.

The OH emission is through a vibrational-rotational transition within the ground state of the hydroxyl. For any vibrational state above 6 the first reaction will be the dominant producer of the hydroxyl but for the levels below 6 both of the OH producers will be important in its production. Since the transition needed here is with is the $v=6\rightarrow2$ transition, both of these reactions are important in the production of the emissions being measured.

The temperatures that are derived using the method described in the next section are rotational temperatures. The reason why these temperatures can be inferred to correlate to the atmospheric temperature where the emission originates from is because of the long lifetime of the transition. This lifetime is longer than the collision frequency between the gas particles. When this happens the molecule is said to be thermalized as it comes into thermal equilibrium

with the rest of the neutral gas surrounding it. Hence the rotational temperatures of the OH transition can be used to measure the temperature of the neutral gas [Sivjee and Hamwey 1987].

3.3 OH(6-2) TEMPERATURE DERIVATIONS

Spectra from the near infrared CCD spectrometer were used to obtain the intensities and temperatures of the hydroxl. Figure 3-2 shows a calculated volumetric emission profile for the OH airglow with two separate modeling methods. The SG98 model refers to the profile obtained from Swenson and Gardner [1998] with the profile from the Full-Wave model obtained by Hickey and Yu [2005].

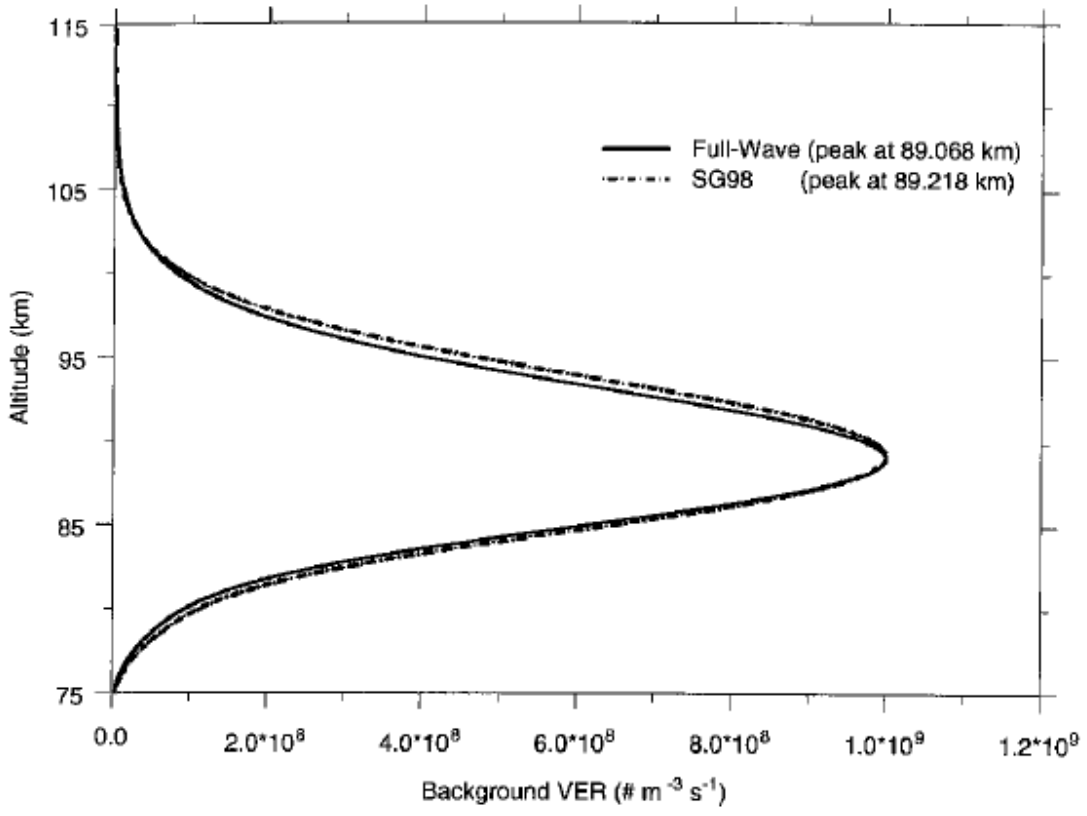

Figure 3-2: Calculated OH Volume Emission Rate for two separate models

[Hickey and Yu, 2005]

The altitude at which the hydroxyl emits the most light is situated in a layer that is located at an altitude of approximately 87km. Since this is the altitude where it is the brightest, the emission that is seen from the ground would primarily be from there. The temperatures at this layer are obtained by analyzing the emissions from nuclear vibrational-rotational dynamics of OH. The photon-flux from each vibrational-rotational radiative transition (J) is related to OH molecular parameters as follows [Sivjee and Hamwey 1987]

$$F(J) = N_o A(J)(2J+1)e^{\frac{-\hbar c W(J)}{kT}} \qquad \text{Equation 35}$$

Hence:

$$\ln\left(\frac{F(J)}{(2J+1)(A(J))}\right) = \ln(N_o) - mW(J) \qquad \text{Equation 36}$$

where $m = \frac{\hbar c}{kT}$, $A(J)$ is an Einstein coefficient for radiative transition, $(2J+1)$ is the degeneracy factor, $W(J)$ is the energy gas between nuclear rotational energy levels, $\hbar$ is Planck's constant, c is the speed of light, k is the Boltzmann constant and T is the neutral air temperature. A plot of $\ln\left(\frac{F(J)}{(2J+1)(A(J))}\right)$ versus $W(J)$ should lead to a straight line whose slope is equal to

$$m = \frac{\hbar c}{kT}. \qquad \text{Equation 37}$$

Figure 3-3 shows a plot of the analysis method for deriving the rotational temperatures from the spectra of the OH airglow. The top part of the plot is the spectra obtained from the instrument with the peaks of the OH(6-2) band located. The brightness of each of these peaks is used in Equation 36 and a linear least-squares fit is done. The slope of this fit is then used to solve for the rotational temperature of the band using Equation 37. The rotational temperature can then be inferred to be the neutral air temperature because the relaxation time of the reaction is long, which allows for the molecule to thermalize with the atmosphere.

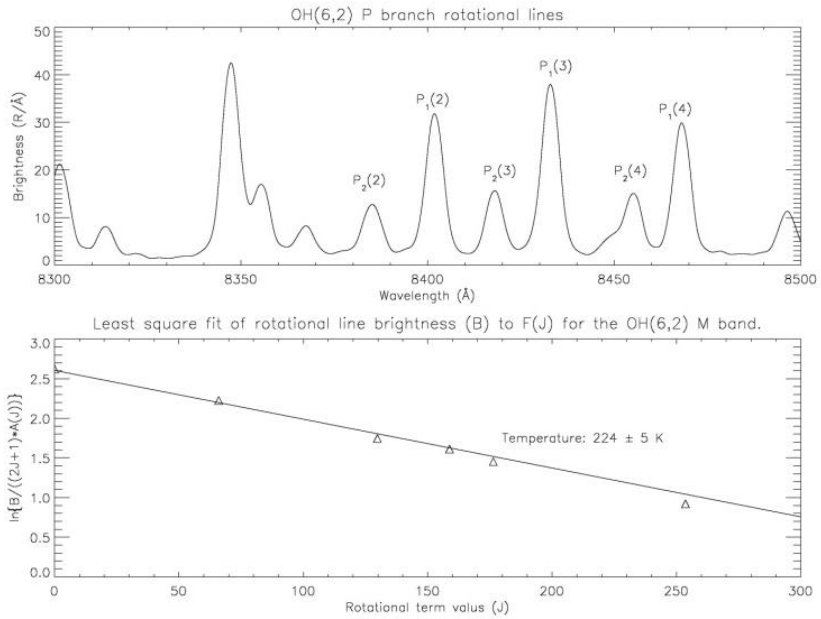

Figure 3-3: OH Analysis Method

3.4 O_2(0-1) CHEMISTRY

The process for the creation and emission of the O_2 Atmospheric (0-1) band from atomic oxygen is shown in the following chemical reactions [Hickey, Schubert and Waltersheid, 1993],

$$O + O + M \rightarrow O_2(b^1\Sigma) + M, \qquad \text{Equation 38}$$

$$O_2(b^1\Sigma) \rightarrow O_2 + h\upsilon, \qquad \text{Equation 39}$$

where *O* is atomic oxygen, *M* is some other major atmospheric constituent such as molecular oxygen or nitrogen and O_2 is molecular oxygen. The $(b^1\Sigma)$ after the O_2 signifies an excited state of O_2. Specifically the lower case *b* means that this state is the second energy level above the ground state with a different spin quantum number than the ground. The 1 means that this state has a spin quantum number of 0 and the Σ gives the type of molecular bond that has been formed. Figure 3-4 shows many the many different bands of O_2 and the energy level of each

when compared to the lowest energy ground state. The $(b^1\Sigma)$ represents the atmospheric band of O_2 and is the second energy level above the ground state.

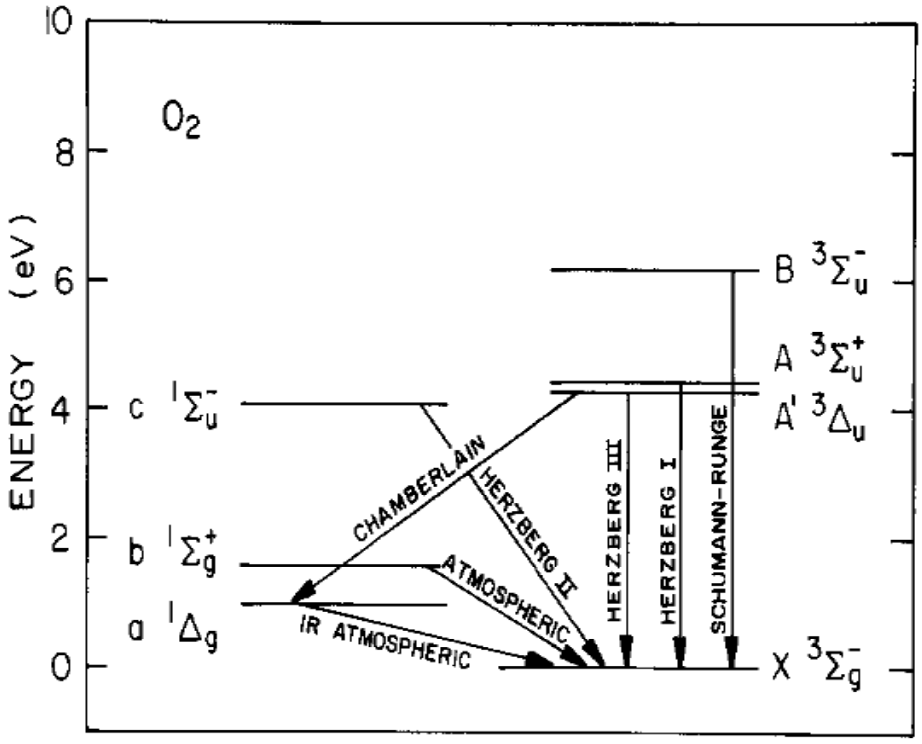

Figure 3-4: Energy Level Diagram for O2 [Chamberlain, 1987]

The second reaction is describing this excited state decaying and releasing a photon. Similar to the OH temperatures, this reaction is slow enough so that the excited oxygen state will thermalize with the surrounding neutral atmosphere. This allows a temperature to be derived which represents the temperature of the atmosphere at that time.

3.5 O_2(0-1) TEMPERATURE DERIVATIONS

As seen from the following volumetric emission profile, Figure 3-5, the molecular oxygen volume emission profile peaks at about 95km.

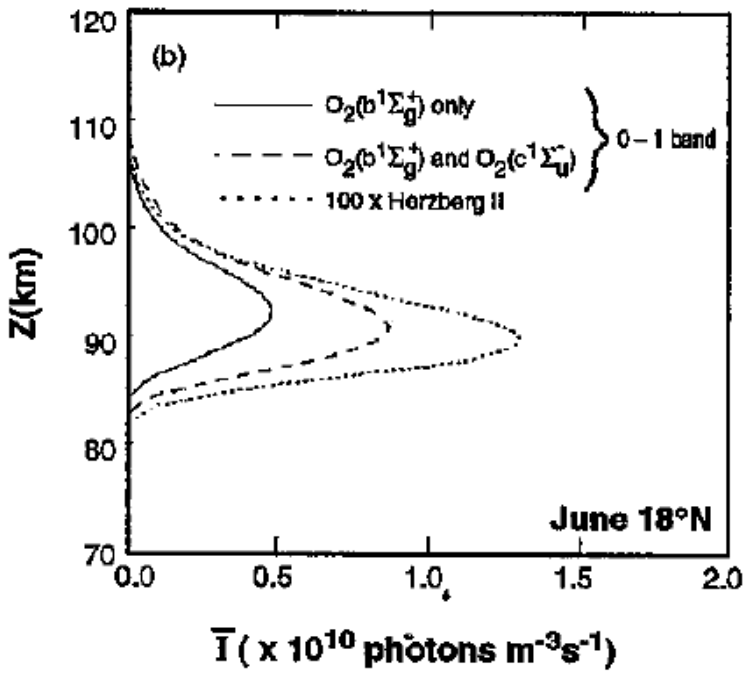

Figure 3-5: Calculated O_2 Volume Emission Rate for 0-1 band

[Hickey, Schubert and Waltersheid, 1993]

Due to the multitude of energy levels within the molecular bond of oxygen, the spectral lines from it are very close together and as a result we are unable to completely resolve the separate lines. Instead of having many different lines the spectrum shows what seems to be two very broad lines situated between the OH(6,2) and OH(7,3) bands. As a result the rotational temperatures are obtained by fitting a theoretical synthetic spectrum of O_2 emissions for different air temperatures and brightness' to the observed data. By iteratively varying the temperature and brightness in the synthetic spectrum the best fit possible is obtained when compared to the observed data. A best fit is defined to be the smallest chi-squared error between the observed data and the synthetic curve. The line brightness of the O_2 atmospheric band as a function of rotational temperature are determined by using the Honl-London factors of Schlapp [1937]. This enables rotational temperatures for the O_2(0-1) band to be obtained as shown in Figure 3-6. The model that was used to derive the temperatures and the brightness' was given to the Embry-

Riddle Space Physics Research Laboratory (SPRL) by Dr. Sam Yee of the Applied Physics Laboratory (APL). This model was also used to derive the same O_2(0-1) temperature in Yee, Niciejewski and Luo [1991].

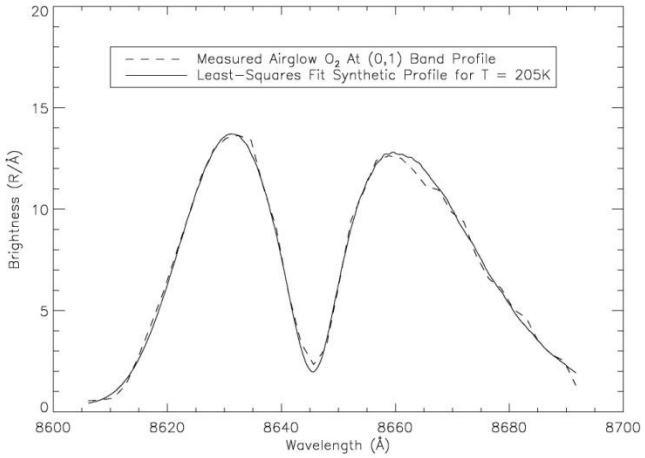

Figure 3-6: O2 Analysis Method

3.6 DATA FILTERING TECHNIQUES

During the process of deriving the temperatures for all of the available scans, several error parameters were calculated and stored for later processing. Both the OH and O_2 methods calculated a χ^2 error, a correlation coefficient as well as error bars for the temperatures. The brightness error for the OH was unable to be calculated because information about the error functions for the spectrometer that was used to collect the data was not available. The χ^2 and the correlation coefficient for the OH were derived from how the points on the plot of $\ln\left(\frac{F(J)}{(2J+1)(A(J)}\right)$ versus W(J) fit along the line of linear-least squares best fit. The O_2 method calculated these between the observed data point on the spectrum and the non-linear synthetic profile. If these points were too scattered away from the best fit line and larger error was found, the scan was not included in the final analysis. If all of the points were closely aligned to the line

then the scan was considered good and hence the temperature was considered correct. The IDL code that analyzed the OH temperatures did not give a temperature error but it was able to be independently derived from the standard deviation that was given for the slope of the fitted line through a propagated error analysis. Using Equation 42 to solve for the temperature gives an equation involving a constant divided by the slope of the line where the constant $\left(\frac{\hbar c}{k}\right)$ is equal to 1.44. The propagated error for an equation with an inverse relation is as follows:

$$\sigma_T = 1.44 * \frac{\sigma_m}{m^2}, \qquad \text{Equation 40}$$

where σ_T is the standard deviation of the temperature, m is the slope of the best fit line and σ_m is the standard deviation of the slope given from the linear regression fit. Figure 3-7 shows an example of what is considered a good fit and what is considered a bad fit. The left hand plot shows all of the points aligning very closely with the best fit line and a correlation coefficient of 0.99 so the temperature derived from this plot is considered true. The right hand plot shows the points scattered about the best fit line with a correlation coefficient of 0.78 which means that the temperature derived from this plot is not considered to be representative of the neutral temperature of the atmosphere.

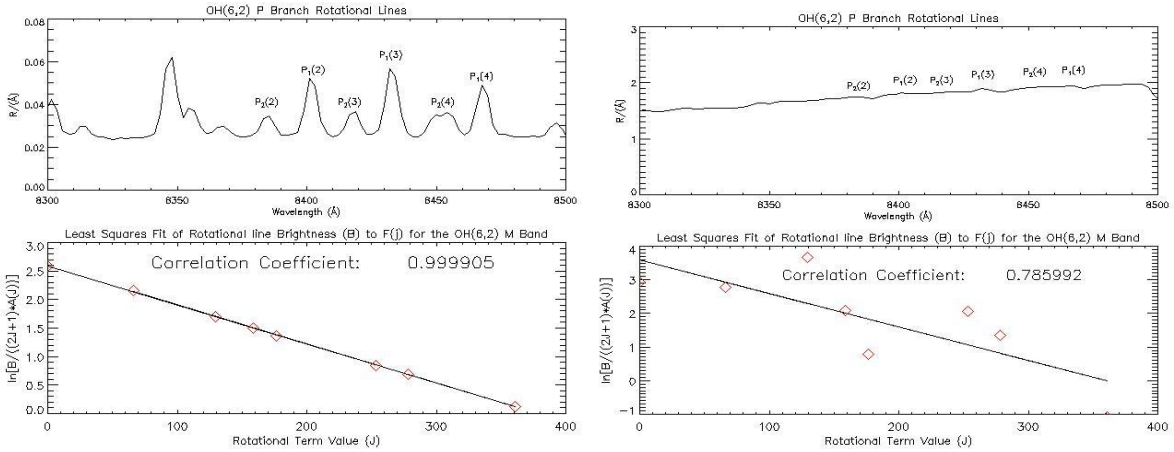

Figure 3-7: Good Correlation (Left) and Bad Correlation (Right)

The O_2 analysis method allowed for error bars to be found for both the temperatures and the brightness' directly along with a reduced chi squared error and a correlation coefficient for the fit with the synthetic profile. It was difficult finding out the exact way the C code derived these errors due to it being given to us by someone not affiliated with the Lab and not having any documentation or very many comments. Upon analyzing the code in detail it was found that the errors are calculated from the curvature of the error surface which is represented by the Jacobian matrix of partial derivatives. Using this method the errors from the fit for brightness and temperature were calculated and stored for later filtering.

Finding the various limits of acceptable errors for the O_2 involved observing how the fitted synthetic spectrum compared with the observed spectrum for many different scans. As the temperature derivation was run, a plot of the observed O_2 spectrum with the synthetic O_2 spectrum on top of it was displayed. The entire spectrum was displayed below that for identification of auroral activity and any bad scans that went through the initial filtering in the C code. Auroral activity needs to be filtered out because it has an O_2 component to it. When the activity occurs the spectrometer will not only see the emission from the kinetic temperature of the O_2 at 93km but from the auroral component of the O_2 emissions. (Sivjee, Shen, Yee, 1999) These plots were also saved in postscript files for later review.

The reduced chi squared error was the first filtering parameter that was used defined as follows:

$$\chi^2_{red} = \frac{1}{N}\sum_{i=1}^{N}(Observed\ point_i - Synthetic\ Point_i)^2, \qquad \text{Equation 41}$$

where *N* is the number of data points in the spectrum. Unfortunately, it became apparent that this was not the best error to filter by itself for the O_2 because there were several scans in which

several solar absorption lines began to show within the *P* branch of the band. Normally this would cause the reduced χ^2 error to become large, but sometimes the absorption occurred during times of low intensity across the entire spectrum as seen in Figure 3-8. In these cases, the difference between the observed point of the spectrum and the synthetic points are very small so the reduced chi squared error drops below 1, which usually indicates a good fit for these cases based upon comparisons of the fits and the calculated χ^2 errors. Since the model is also attempting to fit these solar absorption lines in the model for the O_2 the best fit temperature and brightness cannot be trusted to be the actual rotational temperature of the band. At first this was not noticed because the C code had a line in which it rejected a scan with a reduced chi squared above a certain point so it just skipped it and went to the next scan. After specifically looking for these types of scans and seeing that they were being skipped, it was decided to store all the data for all of the possible scans and to do the filtering in post-processing. Another error parameter was needed to correct for this so a correlation coefficient was used.

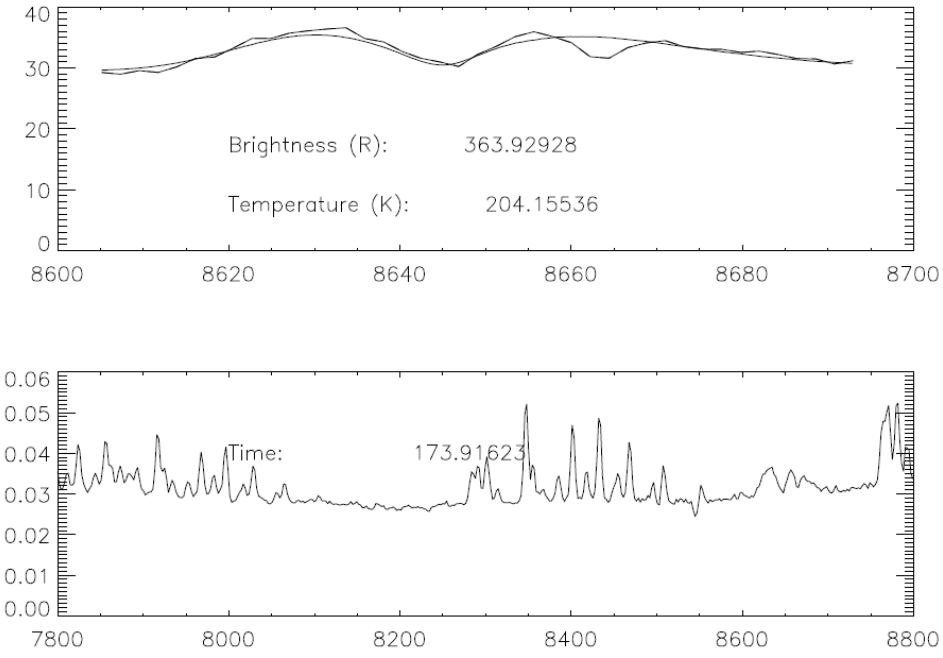

Figure 3-8: Bad Correlation Coefficient of 0.8802 and Good Reduced Chi Square of 0.90424

The correlation coefficient used by IDL is the Pearson Correlation Coefficient defined as

$$r = \frac{\sum_{i=1}^{N}(X_i - \bar{X})(Y_i - \bar{Y})}{\sqrt{\sum_{i=1}^{N}(X_i - \bar{X})^2}\sqrt{\sum_{i=1}^{N}(Y_i - \bar{Y})^2}}, \qquad \text{Equation 42}$$

where X_i are the values in the first data set, observed points in this case, Y_i are the values in the second data set, synthetic points here, and $\bar{X}$ and $\bar{Y}$ are the mean values of each [Computing the Pearson Correlation Coefficient, 2003]. When the observed data and the synthetic data are perfectly correlated the value of the coefficient becomes + 1 or -1. This provides an easy parameter for determining the quality of the fit although it also has a problem with certain types of scans in which a strong 8446 Å line shows within the OH(6-2) band indicating aurora, seen in Figure 3-9. As stated previously the aurora has an O_2 component to it that occurs at a higher altitude than the peak of the airglow layer. Whenever this occurs, the scan will have to be discounted because the analysis is only concerned with gravity waves travelling between the OH airglow layer and the O_2 airglow layer and a temperature derived at a higher altitude would give erroneous results.

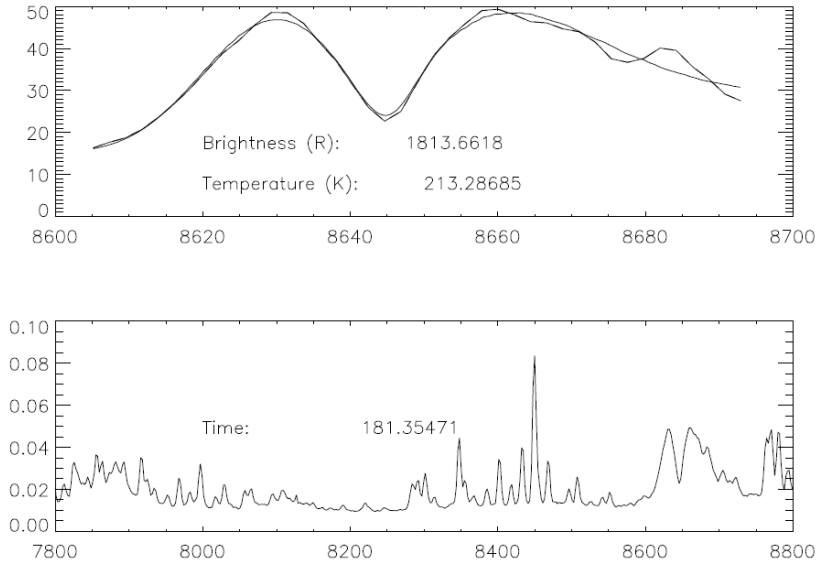

Figure 3-9: Correlation Coefficient=0.98651; Reduced Chi Square=2.29235

The filtering method chosen used both the chi squared error and the correlation coefficient to determine if a scan was considered good or bad. Figure 3-10 shows an example of a scan that was clearly considered to be bad. The χ^2 in this case was 18.8 and the correlation coefficient was 0.67.

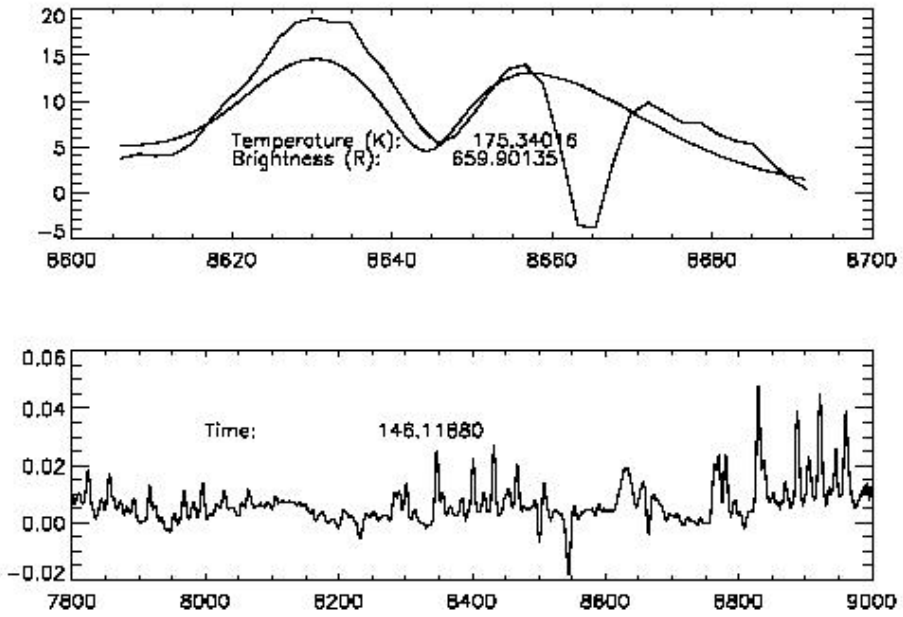

Figure 3-10: Example of "bad" scan. Reduced Chi Square=18.86573; Correlation Coefficient=0.62726

The actual numerical values of the limits for the chi squared error and the correlation coefficient were chosen by visually observing the calculated fits compared to the observed profiles for the O_2 and the OH. For both the South Pole 2002 and 2010 data season the limits on the reduced chi squared error was set to 1, and any scan with a value above this was not included in the gravity wave analysis. The correlation coefficients were set to be 0.95 for the OH and 0.96 for the O_2 based upon comparisons of the least-squares fits and the calculated correlation coefficients. For the solar cycle analysis the data at solar maximum and at solar minimum were needed. The last solar cycle peaked in 2002 and had a minimum in late 2009. Our lab does not have any South Pole data for 2009 due to instrument positioning errors. This was mostly

corrected for the 2010 season so that was used although the recorded intensities were much lower. The OH and O_2 bands were still visible but the magnitudes of the brightness were over 10 times weaker compared to 2002. The data were still usable but would have larger error bars. This time period is still during relatively low solar activity so it will give the required information needed for the analysis. An example of a typical spectrum from the 2002 season is shown in Figure 3-11 and an example of a typical spectrum from 2010 with the reduced brightness is shown in Figure 3-12

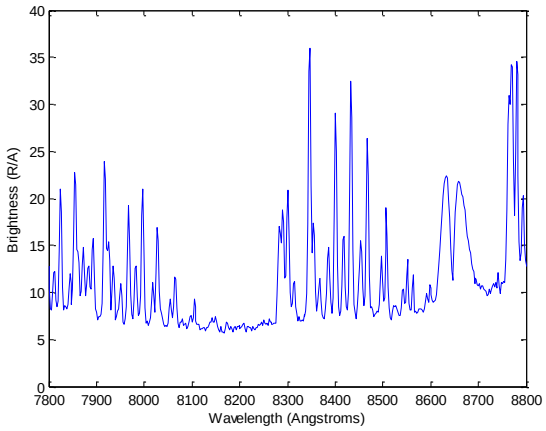

Figure 3-11: Typical South Pole 2002 spectrum

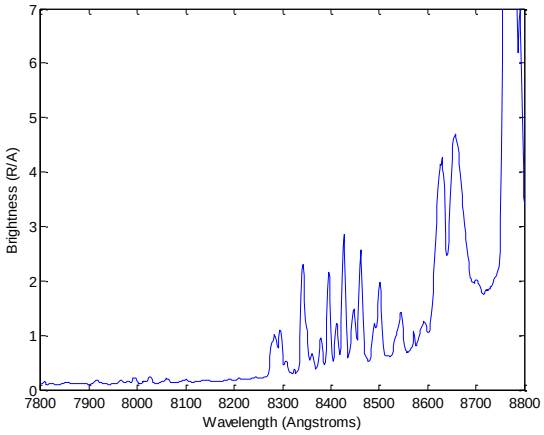

Figure 3-12: Typical South Pole 2010 Spectrum

3.7 SCANNING FOR GRAVITY WAVES

3.7.1 FINDING SIGNIFICANT FREQUENCIES

Identifying gravity waves is a multi-step process that involves several different MATLAB scripts to complete. To begin, the periodicities in the data have to be identified and stored for later use. This was done separately for the OH and the O2 data. The Lomb-Scargle method was used in order to identify any dominant frequencies that occur in a specified time window. The Lomb-Scargle method is very similar to the well-known Fourier transform in that it

transforms a given time series into frequency space. The main difference between the two is that the Lomb-Scargle method does not do a transform of the data and instead attempts to fit a series of sines and cosines to the given data set by a standard least squares fit analysis. The resultant frequencies from this method are then simply the frequencies of the fitted sinusoids. In doing so this method can take a transform of a data set that is not evenly spaced unlike the Fourier transform [Scargle, 1982]. This is ideal for this analysis due to some points being filtered out because they were identified as bad scans or bad fits. This allows the time window to be held constant with no interpolation being done when doing the analysis since missing points do not have to be filled in which may possibly give erroneous results.

While the Fourier analysis is a function that comes with the signal processing toolbox of MATLAB, there is not any function in any of the toolboxes that includes a Lomb-Scargle analysis. A search of the MATLAB Central database gives two scripts that will perform the analysis. The first one, called lombscargle.m is an implementation of the method from Press, Teukolsky, et al. Numerical Recipes, "Spectral Analysis of Unevenly Sampled Data, and coded by Brett Shoelson. While the method is sound, it was written with C programming in mind and as such does not take advantage of MATLAB's matrix functions, which makes it run rather slow. The other script found on the database was simply called lomb.m, and is coded by Christos Saragiotis. It takes the algorithm presented in "Numerical recipes in Fortran 77: the art of scientific computing" by S.A. Teukolsky, W.T. Vetterling and B.P. Flannery and converts it with MATLAB's strengths and weaknesses in mind. After testing, the second script was found to be about twice as fast as the first one. Both of the implementations were confirmed by generating a sample time series with known frequencies and analyzing it with the Fourier method and both of the Lomb-Scargle implementation. All three methods were found to give frequencies within less than 5% of the input frequencies of the sample data.

There is some difference in the output and plotting of these scripts. Specifically the first code has more options in its plotting subroutine and it directly gives the numerical value for several confidence levels such as the 99%, 95%, 90%, and 50%. The second code by comparison has far more simplistic plotting and does not directly give the confidence level values. Instead it gives the confidence level for every point, which means the entire array has to be searched through to find the points which are above the chosen confidence level. Of course this is advantageous in that any level can be specified to analyze. Periodicities with confidence levels above 95% and 90% were stored so that the gravity wave analysis can be completed for the 90% confidence level if the 95% does not give many detected waves. This allows for a balance to be chosen between the number of gravity wave instances and the confidence of those waves from the Lomb-Scargle analysis. Any wave periodicity with a confidence level below the 90% confidence level is not considered to actually be there and due to noise in the data. Performing the analysis with a 95% confidence level was found to give only 20 waves above this level in both years due to random variations in the atmosphere and errors from the temperature derivations so the 90% confidence level limit was used for the analysis.

The choice of data window will affect the amount of waves detected at certain confidence levels. A larger window will typically allow for a larger number of high confidence level detections due to having more data points to work with but would have difficulty giving a high confidence for higher frequency waves. This is because the high frequency waves tend to only last a short amount of time so they become smeared out by the longer lasting lower frequency waves in the larger window. The exact window used was determined by running the analysis for the whole year for several different window sizes and then comparing how many simultaneous waves in the OH and O_2 layers were seen. A window size two times larger than the largest wave period of interest gave the greatest number of simultaneous waves. From these findings two

separate data windows were used for the entire analysis. The first is a two hour window to detect waves with periods less than one hour and the second is a ten hour window to detect wave periods between one hour and five hours. The five hour limit was chosen because one of the atmospheric tides has a period of six hours and this analysis is only concerned with gravity waves. There have also been detections of some three hour tides at the South Pole station, [Patel, 2010], so wave periods close to three hours would have to be cut so as to be certain the analysis does not include any tidal detections.

A Hann window was applied to the data which gives a maximum weight to the center point of the window and goes toward zero at the ends as shown in Figure 3-13. When performing a frequency analysis on a square window, the sudden jumps at the ends in the data will cause what is known as leakage into the analysis. This leakage takes the form of frequencies in the analysis that are not in the data but are only due to the square window not being an exact fit for the frequencies in the data. The windowing reduces this leakage by making the ends of the data smoothly go toward zero. It also allows the waves to be detected at or near the center of the window as the code scans through the time series. A Hamming window is also a common data window used which is very similar to the Hann but does not go to zero at the ends. The equation for the window is as follows with *N* being the number of data points inside the window [Weisstein].

$$w(n) = \frac{1}{2}\left(1 - \cos\left(\frac{2\pi n}{N-1}\right)\right) \quad 0 \le n \le N-1. \qquad \text{Equation 43}$$

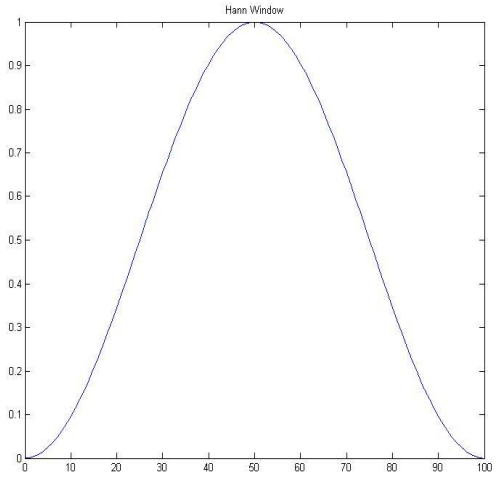

Figure 3-13: Hann Window

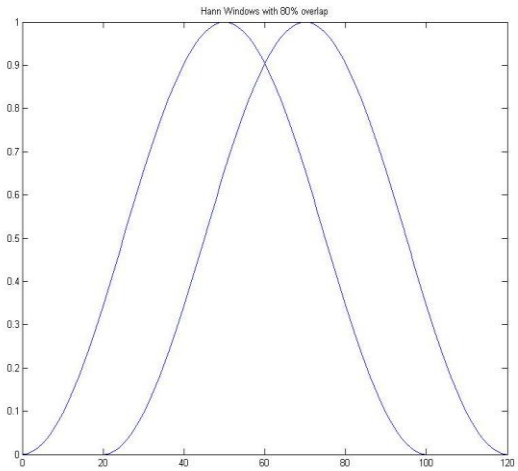

Figure 3-14: Hann Window with 80% overlap

The amount of time to slide the window was set to be have an 80% overlap with the previous one (Figure 3-14). While this would give many of the same frequencies in subsequent windows a simple filtering method described later can pick out the individual frequencies. The high overlap was done to make sure that any fast moving waves are detected in the data sets since they would move through the layer quickly and might not be seen at a high confidence level if they are on the left or right side of the peak of the Hann window. The data are taken at two minute intervals so the smallest period that can be seen from this would be four minutes but some noise was still being seen by the Lomb-Scargle analysis. This was corrected by simply taking 5 minutes as the smallest possible period.

A Savitzky-Golay filter with a five point moving average was used for the ten hour windowed data to smooth the data set for a cleaner signal with the Lomb-Scargle analysis. This is a smoothing method which uses a polynomial fit of degree n to a sliding window of size $2n+1$ to determine the new value of each point. It is useful for this analysis because it preserves the local maxima and minima of each sliding window which can be lost with a simple moving

average smoothing method [Savitzky-Golay, 2010]. The same filter was used to smooth a temperature time series for tidal analysis at the South Pole [Azeem and Sivjee, 2009].

The following table summarizes these various settings. This was done separately for the OH and O_2 brightness' and temperatures for each and stored for later filtering.

Window Size	Smallest Period	Largest Period
2 hours	5 minutes	60 minutes
10 hours (smoothed)	1 hour	5 hours

3.7.2 IDENTIFYING INDIVIDUAL WAVES

The next part of the analysis is to scan through all of the frequencies to pick out times when the same wave period is seen in both layers. Instead of looking at every single wave signature in both layers a MATALB script was created to quickly scan through both sets of data. It will not be possible to have the exact same wave period be seen in both the sets of data due to numerical errors in the analysis so a percent difference limit had to be set in the script so that wave periods that are close to each other can be considered the same wave. This was again determined by simply running the filtering script for several different limits and looking at the results to see which ones gave acceptable results. A 10% difference was found to give waves that are sufficiently close together in frequency.

After the waves in both layers were identified, another script was created to filter out and store the individual waves. Due to the amount of time that the window was slid, the same wave was detected in a few sequential windows. Since a Fourier/Lomb-Scargle analysis does not give any information about the time that the wave occurs, only if it occurs in that particular window, the same wave period could be seen if it occurs in one location of one window or in another

location of the next. This new filter was made so that it would scan through the previous results and store the center window that the particular wave period was seen. For example, if the same wave period was seen in 5 sequential windows then the 3rd one would be stored so that it would be in the center of the Hann window and hence have the greatest weight compared to the rest of the data in the window.

3.7.3 AMPLITUDES AND PHASES OF THE WAVES

After individual waves were isolated, each of the wave's vertical wave properties were obtained using both a wavelet analysis and a least-square sine-cosine fit. The least-square fit of the wave was performed using a sine and cosine series of the form,

$$U = A + \sum_{i=1}^{n} N_{1,i} \sin\frac{2\pi t}{T_i} + N_{2,i} \cos\frac{2\pi t}{T_i}, \qquad \text{Equation 44}$$

where T_i are the significant periodicities from the lomb-scargle analysis within that window, $N_{1,i}$ are the amplitude of the i^{th} sine component of the wave and $N_{2,i}$ are the amplitude of the i^{th} cosine component of the wave and U is a general wave function. These were organized so that the wave detected in both layers was always T_1. The other periods were put in so that the model would fit the data better. The fits were done using MATLAB's built in fitting function which also gives several goodness of fit statistics including the R^2 error for the fit. For a particular period the amplitude is simply given as

$$Amplitude_i = \sqrt{{N_{1,i}}^2 + {N_{2,i}}^2}. \qquad \text{Equation 45}$$

And the phase of the wave from a trigonometric identity for a sine basis wave is

$$\Phi_i = \begin{cases} atan\left(\frac{N_{2,i}}{N_{1,i}}\right) \; if \; N_{1,i} >= 0 \\ \pi - atan\left(\frac{N_{2,i}}{N_{1,i}}\right) \; if \; N_{1,i} < 0 \end{cases} \qquad \text{Equation 46}$$

3.7.4 VERTICAL PROPAGATION FOR WAVES DETECTED IN BOTH LAYERS

The phase and amplitude were found separately for the OH and O_2 temperature and brightness data sets so that amplitudes and phases for each can be derived. The phase difference would simply be the difference between the phase of the wave in one data set and the phase of the wave in the other. Based upon previous modeling results [Hickey and Yu, 2005; Hickey, Schubert and Waltersheid, 1993] the OH layer is located at an altitude of 87 kilometers and the O_2 layer is located at about 94 kilometers. Knowing this information and the phase differences of the waves allows the vertical wavenumber of a particular wave to be calculated given by

$$U(z,t) = U_0 \sin(\omega t + \Phi) = U_0 \sin(\omega t + mz) \qquad \text{Equation 47}$$

$$U(z + \Delta z, t) = U_0 \sin(\omega t + \Phi + \Delta\Phi) = U_0 \sin(\omega t + mz + m\Delta z) \qquad \text{Equation 48}$$

$$m = \frac{\Delta\Phi}{\Delta z} = \frac{phase\ difference}{change\ in\ altitude} \qquad \text{Equation 49}$$

$$\Delta\Phi = \Phi_{OH} - \Phi_{o_2} \qquad \text{Equation 50}$$

where $U(z,t)$ is the wave function, U_0 is the amplitude of the wave, ω is the wave frequency, m is the vertical wavenumber, Φ is the phase of the wave at a particular altitude, z is the altitude, $\Delta\Phi$ is the phase difference due to the altitude difference, Δz is the altitude difference, Φ_{OH} is the phase of the wave in the OH layer and Φ_{o_2} is the phase of the wave in the O_2 layer. The value of m is negative for a wave with downward phase progression and upward energy propagation. The vertical wavelength is then found by

$$\lambda_z = \frac{2\pi}{|m|}, \qquad \text{Equation 51}$$

where the absolute value of the vertical wavenumber is taken so that the wavelength would be a positive value.

3.7.5 VERTICAL PROPAGATION FOR WAVES DETECTED IN ONE LAYER

For waves that were detected in a single layer, the method from Resin and Scheer [1996] was used. Instead of using only temperature or brightness, this method uses derivations from Tarasick and Hines [1990] to find the vertical wavelength of a propagating gravity wave using both the brightness and temperature of a single airglow layer (Equation 30). The Krassovsky ratio for this relation was found by using the amplitude of the wave in the brightness and temperature and the time averages of each in a 24 hour window around the time the wave was detected. As in Resin and Scheer, the phase angle of the Krassovsky ratio was taken to be the difference between the phase of the brightness oscillation and the phase of the temperature oscillation (Equation 29). The vertical wavenumber was then found from the definition for wavelength in Equation 51.

3.7.6 CHECK WITH WAVELET ANALYSIS

The wavelet analysis was used as a check on the automatic Lomb-Scargle script so that the waves that were detected were assured to be real. The wavelet MATLAB script provided was by C. Torrence and G. Compo of the University of Colorado, Program in Atmospheric and Oceanic Sciences and is available at http://paos.colorado.edu/research/wavelets/. The wavelet analysis was plotted and checked by eye to see if the dominant frequencies seen in the Lomb-Scargle analysis were also seen in the wavelet analysis which also allowed for a visual check on the interpolated and smoothed data. A Morlet wavelet seen in Figure 3-15, was chosen for the

wavelet analysis because its shape has a maximum in the center with zeroes toward the ends. This behavior correlates well with the signature of a wave passing through an airglow layer. The input wavenumber for the Morlet wavelet was taken to be 30 with two minute time intervals chosen based upon the data sampling time. A wavelet analysis requires the input to have a constant time interval so any data that has gaps has to be interpolated. The filtered brightness and temperature time series has gaps in them so a simple linear interpolation was done with a time interval set to the original time interval of two minutes.

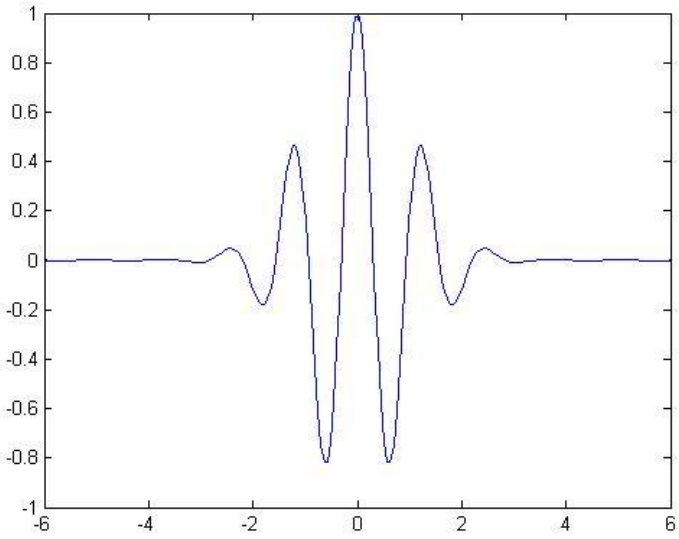

Figure 3-15: Morlet Wavelet

Along with the simultaneous wavelet analysis for both data sets, the windowed data, the Lomb-Scargle periodigram as well as the best fit curve based upon the model equation were all plotted. This was done with each detected wave so as to visually check what the data the program is trying to fit looks like. If the data does not have enough points to produce at least one period then the wave is rejected because the wave that the analysis detects could just be a simple jump in the temperature due to some other event and not a gravity wave.

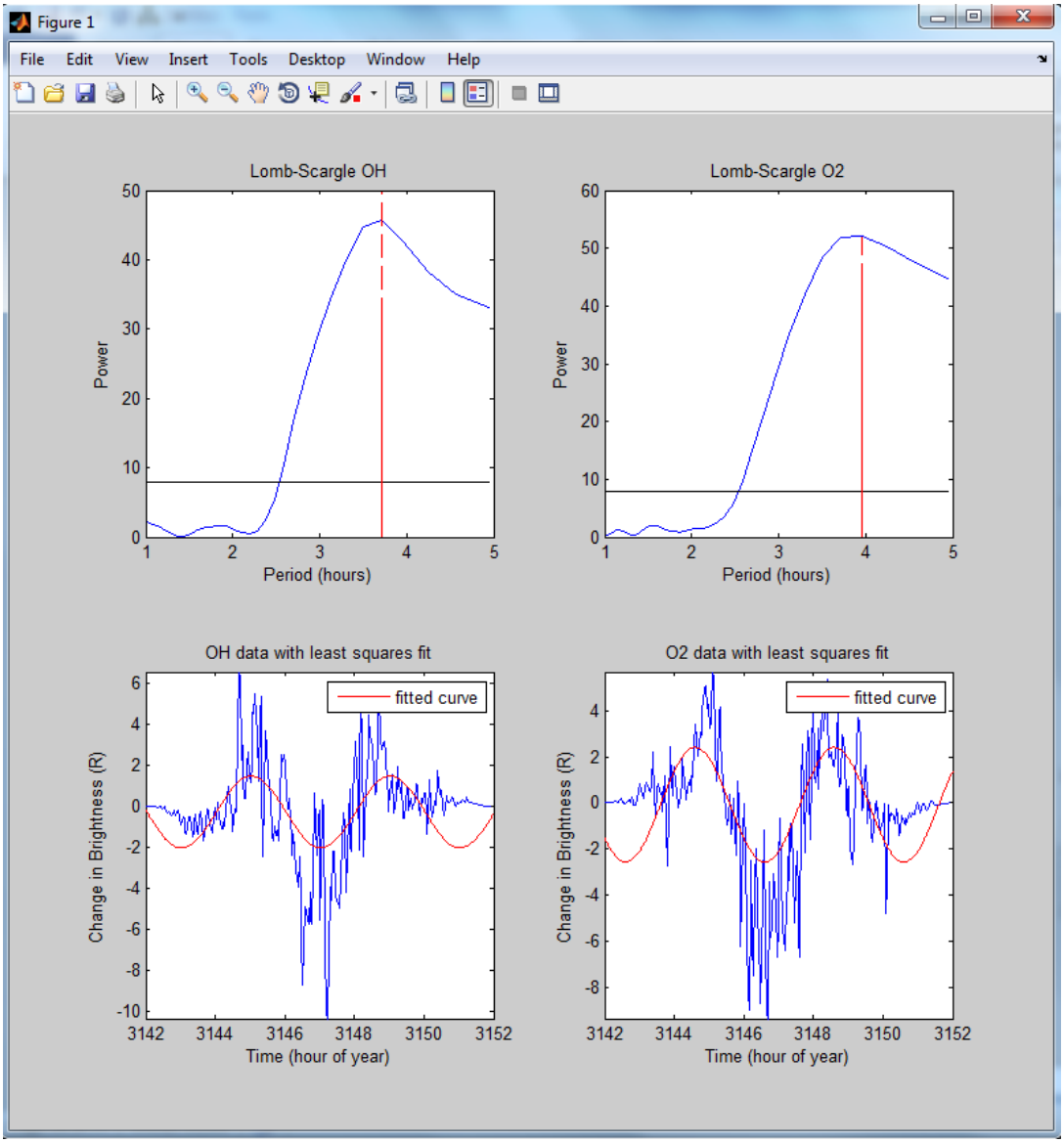

Figure 3-16: Analysis Method Window 1

The vertical dashed line in the Lomb-Scargle windows indicate the detected wave period in each data set. The horizontal black line in the Lomb-Scargle windows are the 90% confidence level; any peak above this line is above this confidence level. The windowed data and change in brightness from the average are plotted in the lower two windows. The fitted wave is with all significant periodicities included.

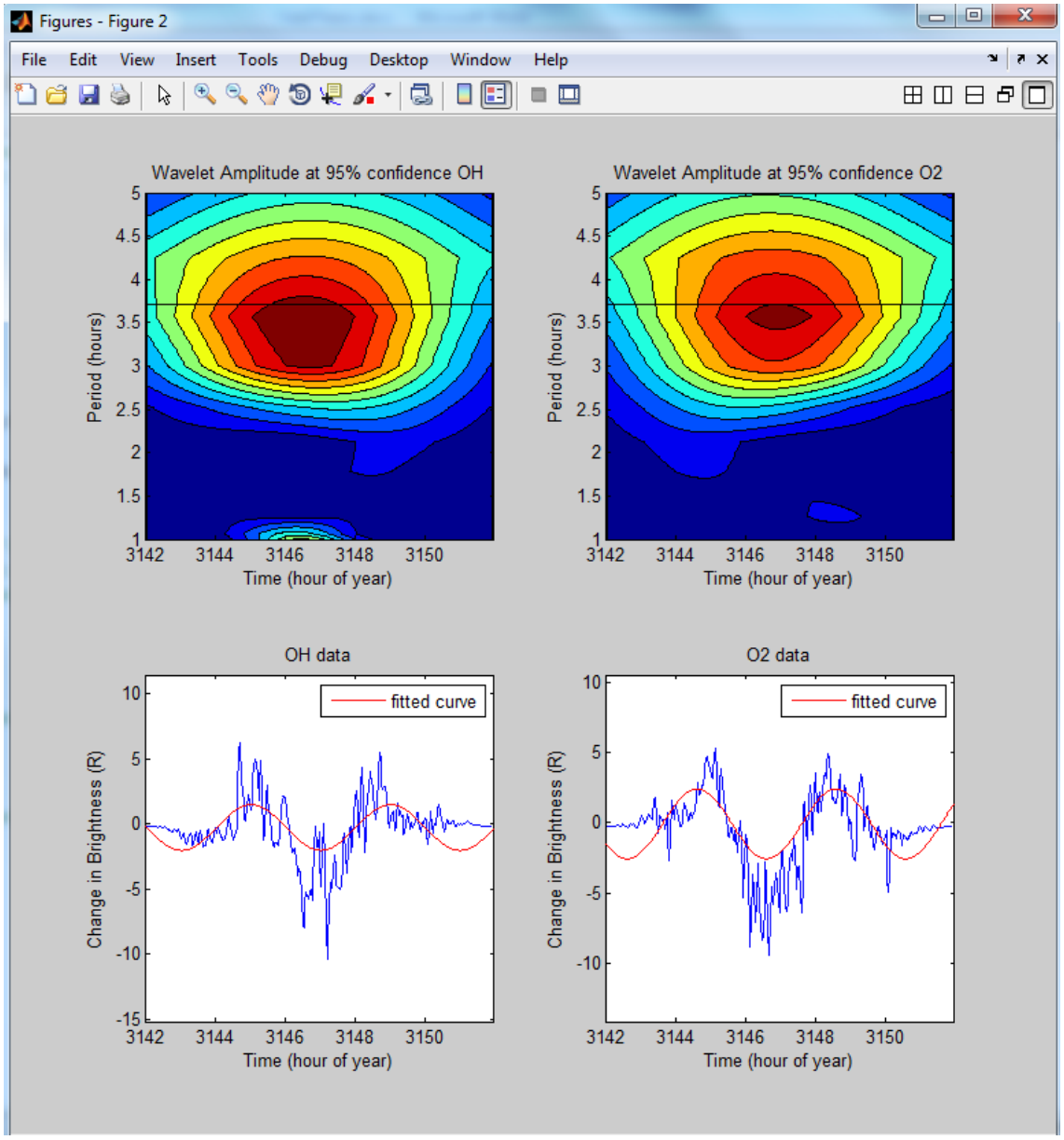

Figure 3-17: Analysis Method Window 2

The contour plots give the wavelet analysis results with the black horizontal line the detected wave period from the Lomb-Scargle analysis. The lower plots give the same data as before but with only the interested wave period fitted. This is done to see how this particular wave period fits to the data and to give a sense of where it fits best within the window.

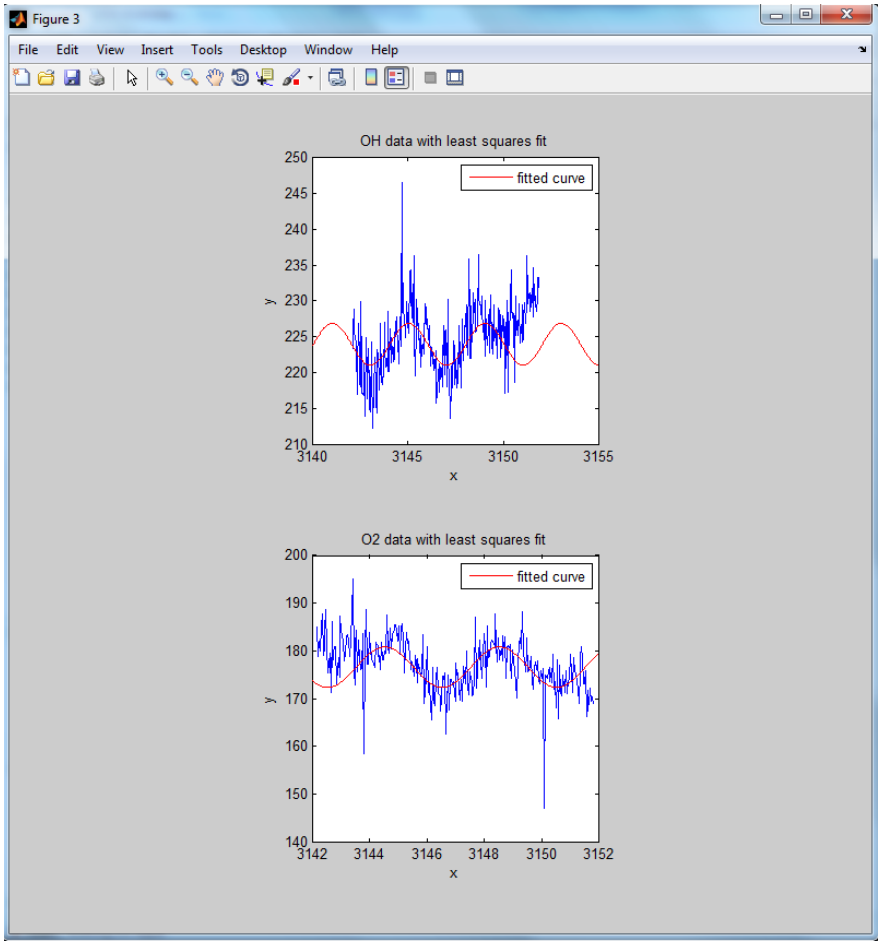

Figure 3-18: Analysis Method Window 3; Raw data fits

With the best fits for the entire window displayed the detected wave in both layers was searched for within the window. Sometimes the wave would not last throughout the window and a best fit would under or overestimate the amplitude of the actual wave. In this case the beginning and end of the wave in the window was chosen and a new best fit was done on the new smaller window using the original non-smoothed data (Figure 3-18). The new amplitude and phases were then stored. The phase difference was also used to filter out any evanescent waves that were detected due to them not having any vertical propagation. They are identified by having either a zero or π phase difference and a range of ± 0.2 radians from these was set as the limits for rejection.

3.7.7 GRAVITY WAVE POST-PROCESSING

These results were then analyzed to derive several gravity wave parameters using theoretical results. Using the gravity wave dispersion relation with constant background winds (Equation 24), the horizontal wavenumber was found. This dispersion relation involves the vertical wavenumber, m, the speed of sound, c, the acoustic cutoff frequency, ω_a, the intrinsic wave frequency, ω, the velocity of a constant background wind, u_0, and the Brunt-Vaisala frequency, N. Only the vertical wavenumber and the intrinsic frequency are known directly, the other parameters are inferred using the NRLMSIS-00 atmospheric model and the Horizontal Wind Model 2007 for the background wind.

The MSIS model describes the neutral temperatures and densities of the atmosphere as a function of magnetic index, F10.7 flux, time, latitude, longitude, and altitude. The model was developed from empirical data from rocket, satellite, shuttle flights and incoherent scatter radar measurements for altitudes above 72.5km. Below this the model is primarily based on the MAP Handbook and averages from the National Meteorological Center. The version of MSIS that is used is the NRLMSIS-00 included in the Aerospace toolbox in MATLAB and developed by Mike Picone, Alan Hedin, and Doug Drob. This is the latest released version of the model and is based on the MISISE-90 model which is freely available online. The main differences between the 00 model and the 90 model is that the 00 model has extensive use of drag and accelerometer data on total mass density, revised O_2 and O in the lower thermosphere , and an additional nonlinear solar activity term. The actual recorded magnetic index and F10.7 fluxes were input along with the required time, latitude, longitude, and altitude needed so as to get an accurate value for the neutral densities [Picone, 2003].

To get the background wind, the 2007 release of the Horizontal Wind Model was used. This is an empirical model for horizontal winds in the troposphere up to the thermosphere. This version was developed by the Space Science Division of the Naval Research Laboratory and includes the data from HWM93 in addition to new ground and space based wind measurements and wind profiles from NASA-UARS/WINDII, NASA-UARS/HRDI, NSF-CEDAR database and lower thermosphere NCEP data. The winds given from the model have a quiet-time and geomagnetically disturbed portions as well as the total winds. The magnetic index for the time of interest as well as the required latitude, longitude, time, and altitude were input with the total winds from the output being the values used for the background wind. [Drob et al., 2008].

The unperturbed total neutral density of the atmosphere is given directly as an output of the NRLMSIS model. The atmospheric pressure was then derived using the ideal gas law with the temperature from the spectrum analysis and the total density from the model. From Equation 17 the speed of sound was then calculated with the ratio of specific heat, γ, being set to 1.4. This allowed for the acoustic cutoff frequency and the Brunt-Vaisala frequency to be calculated which in turn allows for the horizontal wavenumber to be calculated from the dispersion relation. The horizontal wavenumber calculated assumes that the background wind derived from the HWM07 is in the direction of wave propagation. A direction has to be assumed because the actual wave propagation direction cannot be derived from the available data which will affect the value of the calculated horizontal wavenumber. The solution to the dispersion relation gives k to the fourth power which implies four solutions. By definition the horizontal wavenumber is taken to be positive which eliminates two of the solutions. Since $\omega << N$ for all of the detected waves, the smaller of the two horizontal wavenumbers can be taken because the horizontal wavelengths of atmospheric gravity waves are larger than the vertical wavelengths as proven by both theoretical and experimental results [Tarasick and Hines, 1990]. The horizontal wavelength is then

$$\lambda_x = \frac{2\pi}{k}. \qquad \text{Equation 52}$$

With the horizontal and vertical wavenumbers known the phase speeds will be given as

$$c_x = \frac{\omega}{k}, \qquad c_z = \frac{\omega}{m}. \qquad \text{Equation 53}$$

The wave horizontal group velocity, u_g, and vertical group velocity, w_g, can be found by the following equations: [Nappo, 2002]

$$u_g = \frac{\partial \omega}{\partial k}, \qquad w_g = \frac{\partial \omega}{\partial m}, \qquad \text{Equation 54}$$

which are found by solving the dispersion relation algebraically for ω, performing the partial derivatives and then replacing the variables with numerical values. The four separate analytical values of the horizontal wavenumber carry through the derivatives and give four possible solutions for the each group velocity. The group velocity that corresponds to the chosen horizontal wavenumber is used as the calculated group velocity. The analytical expressions are

$$w_g = \pm \frac{\sqrt{2}Nck\left(2c^2m + \frac{4c^2k^2m + 4c^4m^3 + 4m\omega_a^2}{2\sqrt{X + \omega_a^4}}\right)}{2\frac{1}{\sqrt{X}}\left(\sqrt{X + \omega_a^4} + \omega_a^2 + c^2k^2 + c^2m^2\right)^2}, \qquad \text{Equation 55}$$

$$w_g = \pm \frac{\sqrt{2}Nck\left(2c^2m - \frac{4c^2k^2m + 4c^4m^3 + 4m\omega_a^2}{2\sqrt{X}}\right)}{2\frac{1}{\sqrt{\omega_a^2 - X}}\left(-\sqrt{X + \omega_a^4} + \omega_a^2 + c^2k^2 + c^2m^2\right)^2}, \qquad \text{Equation 56}$$

$$u_g = u_0 \pm \sqrt{\frac{2N^2c^2}{\sqrt{X + \omega_a^4} + \omega_a^2 + c^2k^2 + c^2k^2}} \mp \frac{\sqrt{2}Nck\left(2c^2k + \frac{-8N^2c^2k^2 + 4c^4k^3 + 4c^4km^2 + 4c^2k\omega_a^2}{2\sqrt{X + \omega_a^4}}\right)}{2\frac{1}{\sqrt{X}}\left(\sqrt{X + \omega_a^4} + \omega_a^2 + c^2k^2 + c^2m^2\right)^2}, \qquad \text{Equation 57}$$

$$u_g = u_0 \pm \sqrt{\frac{2N^2c^2}{\sqrt{X+\omega_a^4}+\omega_a^2+c^2k^2+c^2k^2}} \mp \frac{\sqrt{2}Nck\left(2c^2k-\frac{-8N^2c^2k^2+4c^4k^3+4c^4km^2+4c^2k\omega_a^2}{2\sqrt{X+\omega_a^4}}\right)}{2\frac{1}{\sqrt{\omega_a^2-X}}\left(-\sqrt{X+\omega_a^4}+\omega_a^2+c^2k^2+c^2m^2\right)^2},$$ Equation 58

Where: $X = -4N^2c^2k^2 + c^4k^4 + 2c^4k^2m^2 + c^4m^4 + 2c^2k^2\omega_a^2 + 2c^2m^2\omega_a^2.$ Equation 59

3.8 EXAMPLE ANALYSIS

For an example analysis the waves seen in Figure 3-16, Figure 3-17, and Figure 3-18 will be used. This wave was first identified from the sliding Lomb-Scargle analysis in both the OH and O_2 brightness time series and stored for the vertical propagation analysis. The least-squares fits of Equation 44 were performed with the following results:

$$\omega = 4.12\text{x}10^{-4}\frac{rad}{s}$$ Equation 60

$$U_{OH} = 223.4 + 3.647 * \sin\frac{2\pi t}{4} - 1.085 * \cos\frac{2\pi t}{4}$$ Equation 61

$$U_{O2} = 176.6 + 3.331 * \sin\frac{2\pi t}{4} - 4.022 * \cos\frac{2\pi t}{4}$$ Equation 62

$$Amplitude_{OH} = \sqrt{3.647^2 + 1.085^2} = 3.8,$$ Equation 63

$$Amplitude_{O2} = \sqrt{3.331^2 + 4.022^2} = 5.2R$$ Equation 64

$$\Phi_{OH} = atan\left(\frac{-1.085}{3.647}\right) = -0.2892rad$$ Equation 65

$$\Phi_{O2} = atan\left(\frac{4.022}{3.331}\right) = 0.8791rad$$ Equation 66

$$\Delta\Phi = -0.2892rad - 0.8791rad = -1.1683rad \quad \text{Equation 67}$$

$$m = \frac{-1.1683rad}{6000m} = -1.947\text{x}10^{-4}m^{-1} \quad \text{Equation 68}$$

$$\lambda_z = \frac{2\pi}{|-1.947\text{x}10^{-4}\ m^{-1}|} = 32.2km \quad \text{Equation 69}$$

The Horizontal Wind Model for this time yields a constant background wind of 24.2m/s. The NRLMSIS00 model was also used to acquire a non-perturbed density of $1.5\text{x}10^{-6}\frac{kg}{m^3}$, and a non-perturbed temperature of 208.5K.The Ideal Gas Equation is the used to get atmospheric pressure, which is then used to get the speed of sound from Equation 17 as shown

$$P_0 = \rho_0 RT = 0.0905\frac{N}{m^2}, \quad \text{Equation 70}$$

$$c = 290.43\frac{m}{s}, \quad \text{Equation 71}$$

$$N = Brunt\ Vaisala\ Frequency = \sqrt{\frac{(\gamma-1)g}{c^2}} = 0.0209\frac{rad}{s}, \quad \text{Equation 72}$$

$$\omega_a = \frac{\gamma g}{2c} = 0.0231\frac{rad}{s}. \quad \text{Equation 73}$$

With these parameters known the horizontal wavenumber can be solved for from the dispersion relation (Equation 26),

$$k = 3.5\text{x}10^{-6}m^{-1}, \quad \text{Equation 74}$$

$$\lambda_x = \frac{2\pi}{k} = 1{,}788km. \quad \text{Equation 75}$$

The phase speeds are then found from Equation 53 and group velocities from Equation 54.

$$c_x = \frac{\omega}{k} = 117.3\frac{m}{s} \quad \text{Equation 76}$$

$$c_z = \frac{\omega}{m} = -2.06\frac{m}{s} \quad \text{Equation 77}$$

$$u_g = 117.3\frac{m}{s}$$ Equation 78

$$w_g = 1.47\frac{m}{s}$$ Equation 79

The following is a summary of the entire analysis in list format for ease of understanding.

1. Gather brightness and temperature time series from observed spectra.
2. Filter data based upon chi squared error and correlation coefficient.
3. Perform sliding Lomb-Scargle analysis on windowed data.
4. Store only unique waves due to the 80% window overlap.
5. Visually inspect detected waves with Lomb-Scargle analysis , Wavelet analysis and a best fit of a sine-cosine wave with detected periodicities.
6. Store only good quality fits.
7. Use gravity wave theory to calculate vertical and horizontal wavelengths, phase speeds and group velocities.

CHAPTER 4 - RESULTS AND DISCUSSION

To compare the various gravity wave properties between the 2002 and 2010 years, bar plots were created in MATLAB with each year side by side for each parameter. Four different detection methods were also used to compare what type of waves can be seen by each method. The first uses the brightness fluctuations for the OH and O_2 layers simultaneously, while the second uses the intensity weighted temperature fluctuations in both layers. The third and fourth method uses the brightness and intensity weighted temperature in one layer in conjunction with the Tarasick and Hines theory to derive vertical and horizontal gravity waves properties. This was done separately for the OH and O_2 airglow layers. There were a total of 110 gravity waves detected in the 2002 season and 112 detected in the 2010 season.

4.1 USING BRIGHTNESS'S IN OH AND O_2 LAYERS

For this method of gravity wave detection, the vertical wavelength was found from Equation 49 and Equation 51, shown in Figure 4-1. The results from both windows (2hour and 10 hour) are combined on the plots. The wave periods ranged from 38minutes to 4.5 hours. Negative vertical wavelengths on the plots are waves with a negative wavenumber. These are waves with downward phase progression with upward energy propagation. The smallest vertical wavelength detected was about 7km for both seasons. Most of the larger wavelengths have a negative value which indicates downward phase progression. There are twice as many waves with downward energy propagation in the 2002 season when compared to the 2010 season. Another difference between the two seasons is that the 2002 season has a few waves with wavelengths greater than 100km while the 2010 season does not have any such waves. Most waves had wavelengths in the 20km-50km range.

The horizontal wavelengths derived from the dispersion relation include the influence of a constant background wind taken from the Horizontal Wind Model 2007 and are all positive due to the manner in which they were defined. Their magnitudes range from around 100km up to 3000km for 2002 and from 100km up to 2000km for 2010. Similar to the vertical wavelengths, there is not a significant difference between the two seasons with 2002 having a few longer waves.

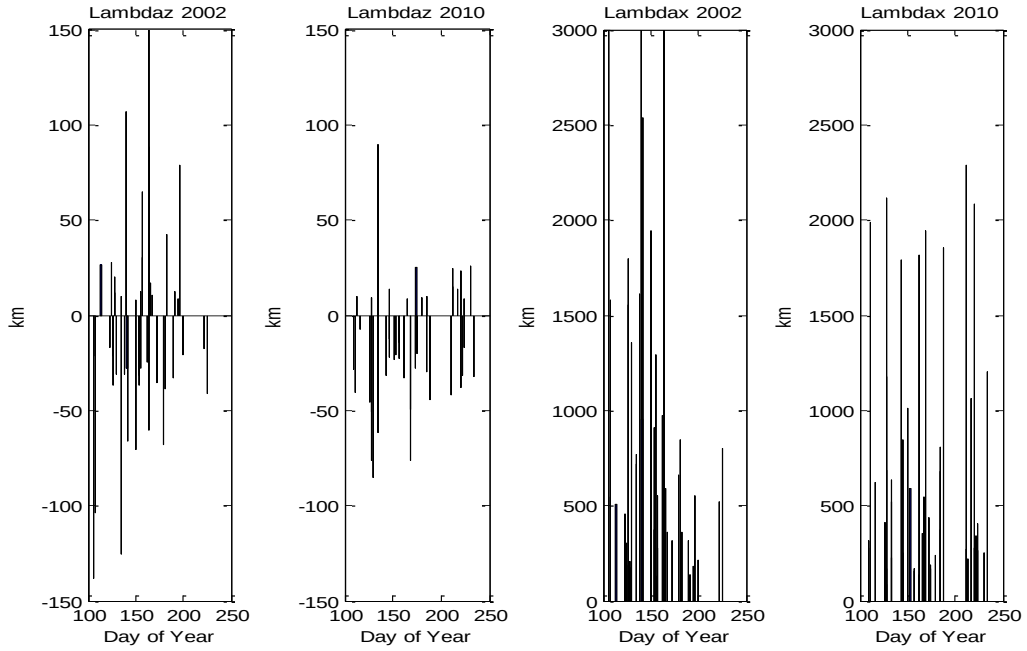

Figure 4-1: Wavelengths with winds included. Negative values indicate negative wavenumber

The phase speeds in Figure 4-2 have both the vertical and horizontal directions exhibiting similar patterns that were seen in the wavelengths. Most of the vertical phase speeds ranged from a few meters per second up to about 30m/s. The 2002 season has three waves with phase speeds greater than this which correspond to the longer wavelength waves. The horizontal phase speeds ranged from 30m/s up to nearly 250m/s.

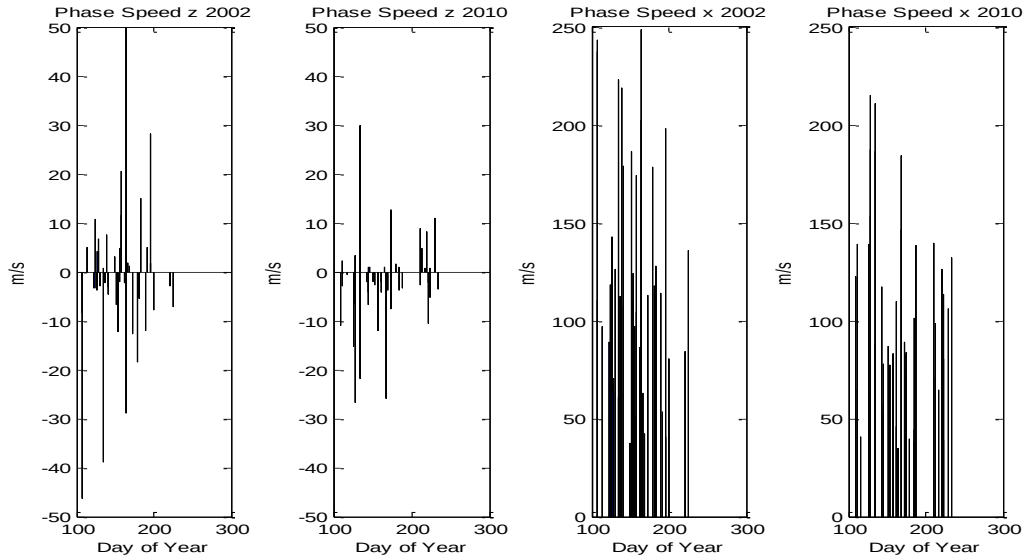

Figure 4-2: Phase Speeds with winds included. Negative values indicate negative wavenumber

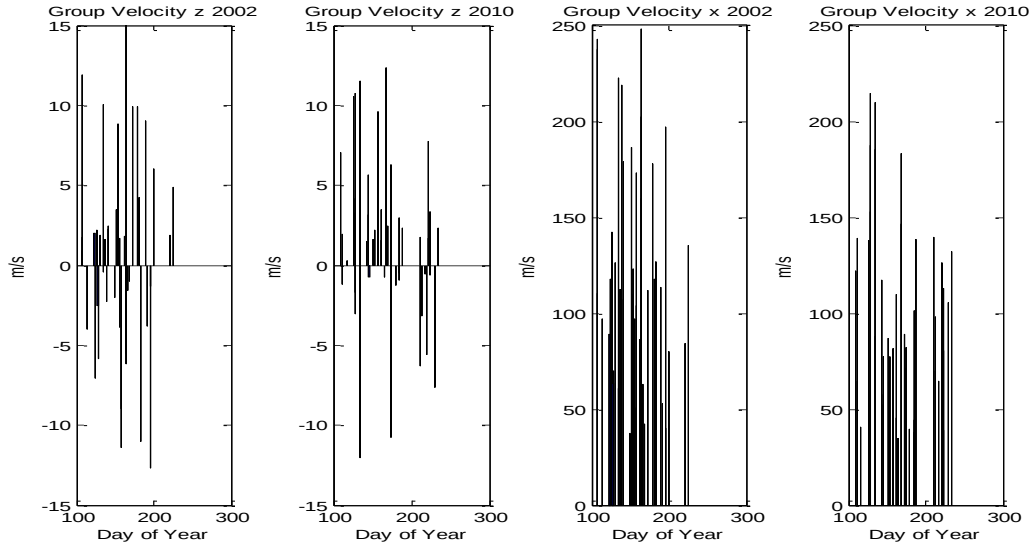

Figure 4-3: Group Velocities with winds included.

The group velocities for the detected gravity waves in Figure 4-3 are all less than 15m/s except one in 2002 which has a group velocity of 17m/s. A positive group velocity in the vertical direction indicates upward energy propagation. Similar to the wavelength results, most waves are propagating upward in both seasons with about 30% propagating downward in 2002 and 18% in 2010.

	2002	2010	Percent Difference from 2002 to 2010
Average detected period	127.0 minutes ±88.1	124.4 minutes ±91.8	-2% ±143%
Average λ_z	55.8km±7.5	40.8km±3.9	-27% ±22%
Average λ_x	1,116.8km±170	960.9km±141.2	-14% ±30%
Average c_z	12.4m/s±2.3	9.3m/s±1.5	-28% ±34%
Average c_x	145.1m/s±9.2	128.4m/s±7.7	-12.2% ±12.3%
Average v_{gz}	5.8m/s±0.76	5.6m/s±0.73	-3% ±26%
Average v_{gx}	144.3m/s±9.15	128m/s±7.7	-11% ±12.3%
% Propagating downward	31%	18%	--

Table 1: Averages of all wave parameters using Brightness between layers

By taking the average of each parameter for each season, seen in Table 1, it can be seen that the magnitudes of both vertical and horizontal components decreased overall from 2002 till 2010. This is still the case even if the wavelengths greater than 100km are not included in the averaging for the 2002 season. Including the standard deviations for each case reveals that the average vertical wavelengths, the average horizontal phase speed and the average horizontal group velocities for the two seasons are more than one standard deviation from each other. The average detected period, the average horizontal wavelengths, the average vertical phase speed and the average vertical group velocity are within a standard deviation so their difference might not be true. Only the average vertical wavelength percent difference did not cross zero with the errors included which means that this is the only difference that can be considered true.

The previous results assumed a constant background wind in the direction of horizontal propagation of the wave. If the background wind is assumed to be in the opposite direction of wave propagation then the only thing that would change in these results is that the magnitudes of

everything but the vertical wavelength would decrease since the vertical wavelength is found directly from the phase difference and does not need the background wind to find it. The same patterns would still be present in the results. Another possibility for the wind is for there to not be any winds during the time that the wave is propagating. This is shown in Figure 4-4 for the wavelengths, Figure 4-5 for the phase speeds Figure 4-6 for the group velocities.

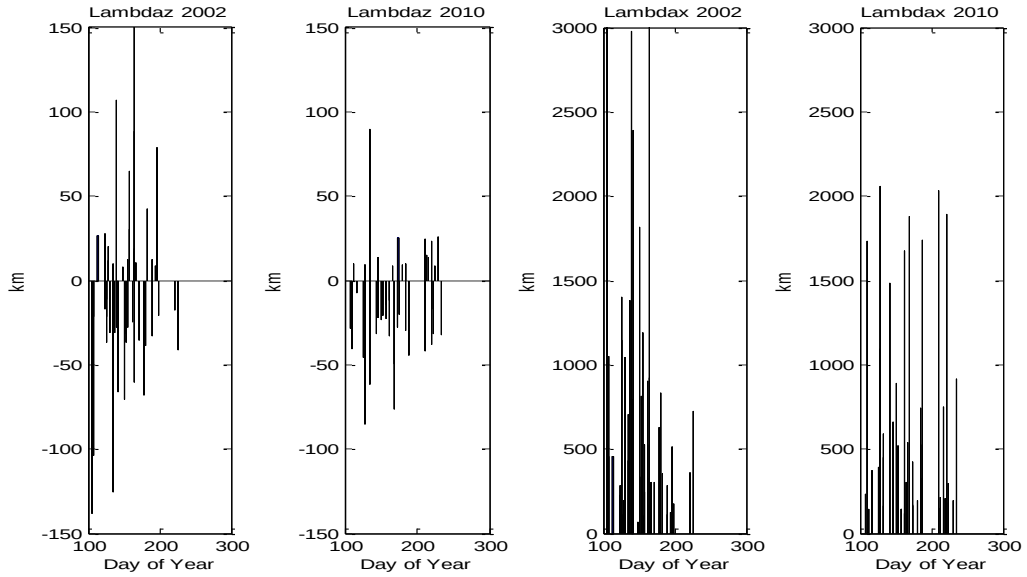

Figure 4-4: Wavelengths without winds. Negative values indicate negative wavenumber

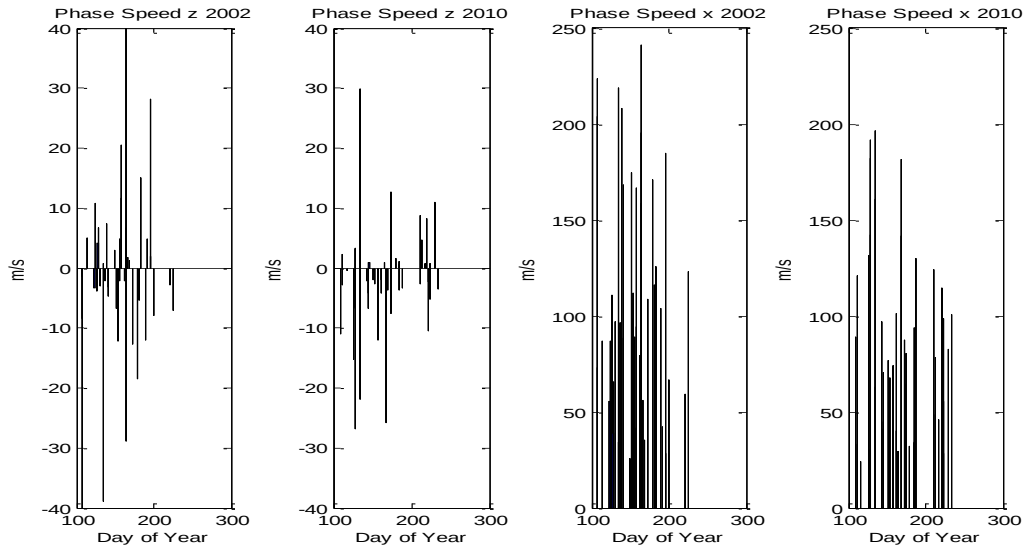

Figure 4-5: Phase Speeds without winds. Negative values indicate negative wavenumber

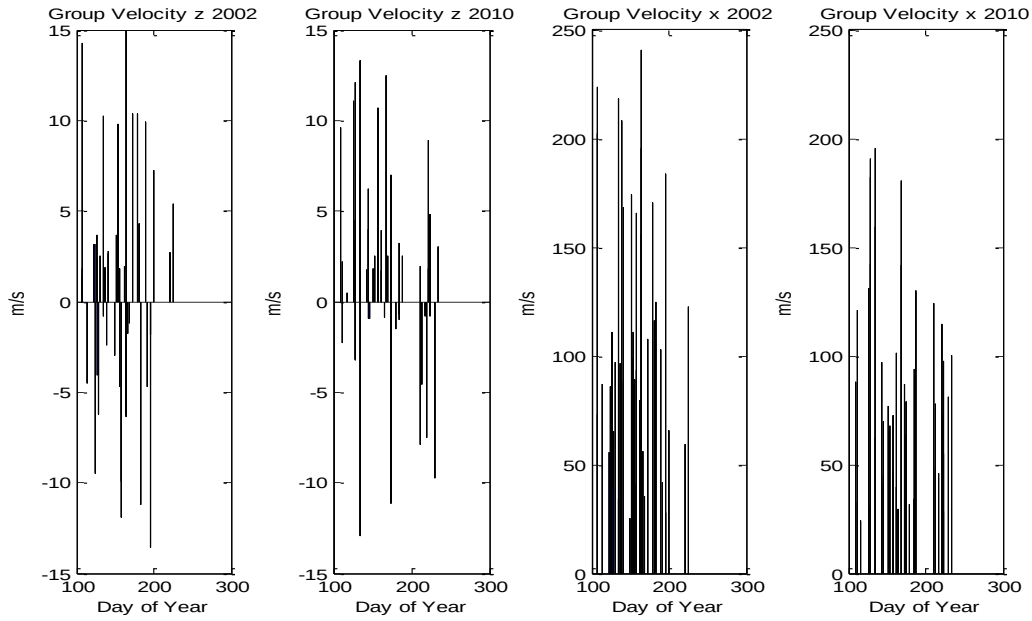

Figure 4-6: Group Velocities without winds

Without the background wind the magnitudes of all of the derived horizontal parameters would only decrease by 5%-10% from the case with the background wind included.

4.2 USING TEMPERATURES IN OH AND O_2 LAYERS

The method used to detect and derive gravity wave parameters in this case are identical to using the brightness's of the airglow layers except that the rotational temperature oscillations are used in both layers instead of the brightness oscillations. Wave periods range from 36 minutes up to 4.5 hours. Some of the detected waves had to be filtered from the final results due to using these temperatures. According to a modeling study by Hickey and Walterscheid [1999], the amplitude of the altitude-integrated volume emission rate weighted temperature perturbation for waves with vertical wavelengths of less than 20km and horizontal phase speed of less than 65m/s differs considerably from the amplitude of the temperature perturbation averaged over the entire emission layer. The amplitude of the altitude-integrated volume emission rate weighted temperature also differs by at least 30% from the amplitude of the temperature perturbations of

the major gasses in the region for waves with vertical wavelengths less than 50km and horizontal phase speeds less than 150m/s. To avoid erroneous results in the analysis these waves were not included in the final results. For the 2002 season this was 30% of the detected waves and 44% of the detected waves in 2010.

Figure 4-7 shows the majority of the waves detected using only the rotational temperatures have a negative wavenumber with upward energy propagation. On average, roughly half of the waves with periods less than 1 hour had a positive wavelength whereas only about 10% of waves with periods greater than 1 hour had positive wavelengths. This is the same for both seasons even with the fewer number of detected waves in 2010. The derived horizontal wavelengths are generally the same for both seasons with a few larger wavelengths found in 2010 which correspond to wave with periods greater than 4 hours.

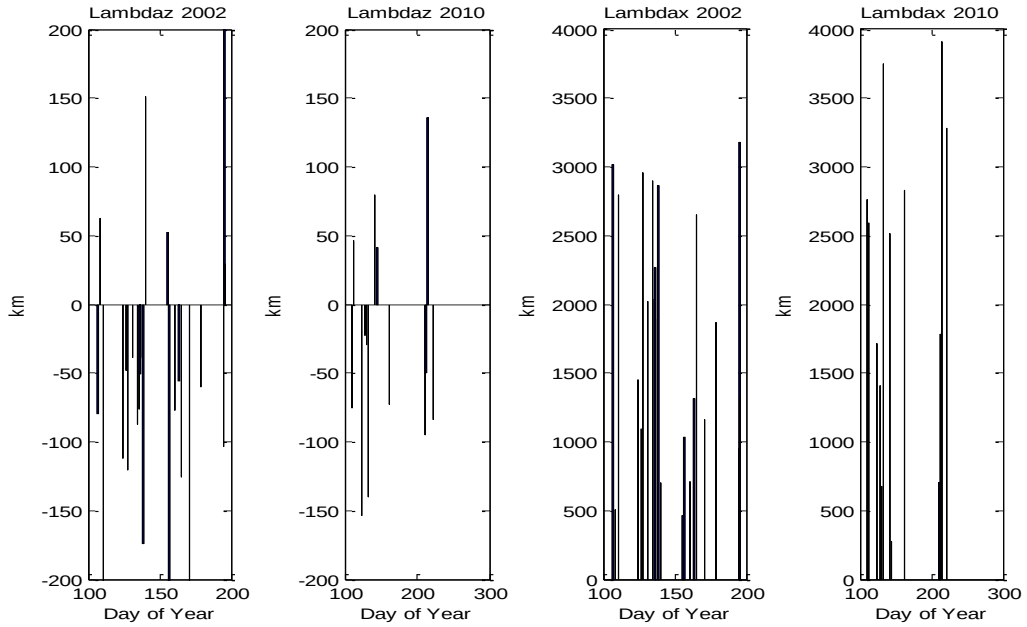

Figure 4-7: Wavelengths with winds included. Negative values indicate negative wavenumber

The phase speeds for these waves are of similar magnitude for the brightness method and are without any large changes between the two seasons, shown in Figure 4-8.

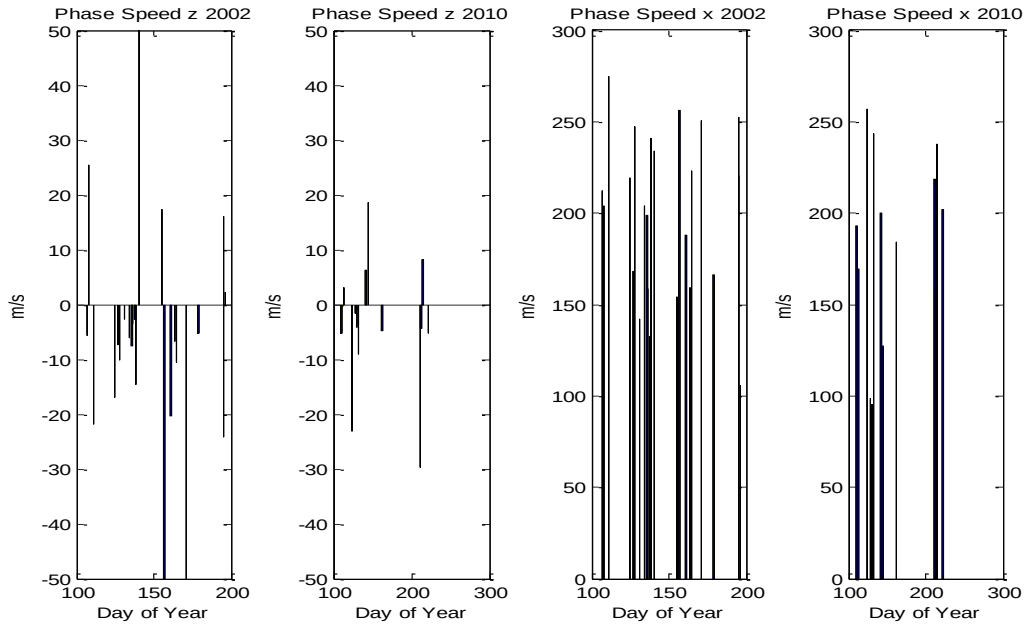

Figure 4-8: Phase Speeds with winds included. Negative values indicate negative wavenumber

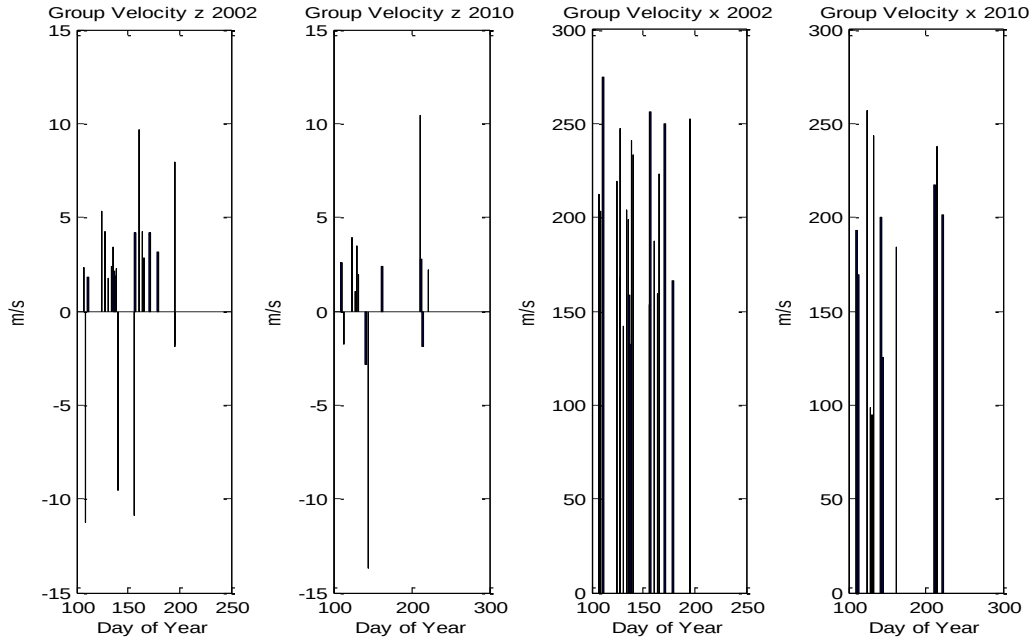

Figure 4-9: Group Velocities with winds included

The group velocities in Figure 4-9 have similar magnitudes to the waves detected using the brightness oscillations between the two airglow layers. These magnitudes are also very similar between the 2002 and the 2010 seasons.

	2002	2010	Percent Difference from 2002 to 2010
Average detected period	151.2 minutes ±70.8	289.7 minutes ±85.7	63% ±69%
Average λ_z	87.3km±10.7	78.8km±11.8	-10% ±27%
Average λ_x	1,808km±203.8	2,169.8km±327	18% ±26%
Average c_z	12.8m/s±2.5	9.5m/s±2.4	-29% ±44%
Average c_x	191.5m/s±9.2	183.3m/s±14.5	4.4% ±%13
Average v_{gz}	4.6m/s±0.74	3.9m/s±1.03	-16% ±42%
Average v_{gx}	191.3m/s±9.2	183.1m/s±14.6	-4.4% ±13%
% Propagating downward	21%	23%	--

Table 2: Averages of all wave parameters using Temperature between layers

Similar to the waves detected from the brightness in the two layers, most of the parameters all decreased from 2002 till 2010 (Table 2). The only exceptions to this are the detected wave periods and the derived horizontal wavelength. The standard deviations on each of the averages show that all of the wave parameters between the two years to be within one standard deviation of each other for this case which means that these differences are not certain enough to draw any meaningful conclusions.

4.3 USING BRIGHTNESS AND TEMPERATURE ONLY IN THE OH LAYER

This method utilizes the Tarasick and Hines theory for gravity wave detection in a single airglow layer using the brightness and the altitude-integrated weighted temperature time series. The wave periods found from this method range from 27 minutes up to 4.5 hours. Using Equation 30 the vertical wavelength was first found followed by the vertical wavenumber. The process for finding the other wave parameters is identical after this. Since the altitude-integrated

temperature is used, the same filtering techniques for wavelengths and phase speeds are used from Hickey and Walterscheid [1999].

Figure 4-10 shows the wavelengths of the detected gravity waves utilizing this method. The two seasons in this case were similar in the magnitude of the vertical wavelengths detected. The 2010 season on average had larger wavelengths when compared to the 2002 season though. The major difference between the two seasons is that a higher percentage of waves were found to be propagating downward in the OH layer in 2010 compared to 2002. The horizontal wavelengths are also very similar for each season as well as with the waves detected using two separate layers.

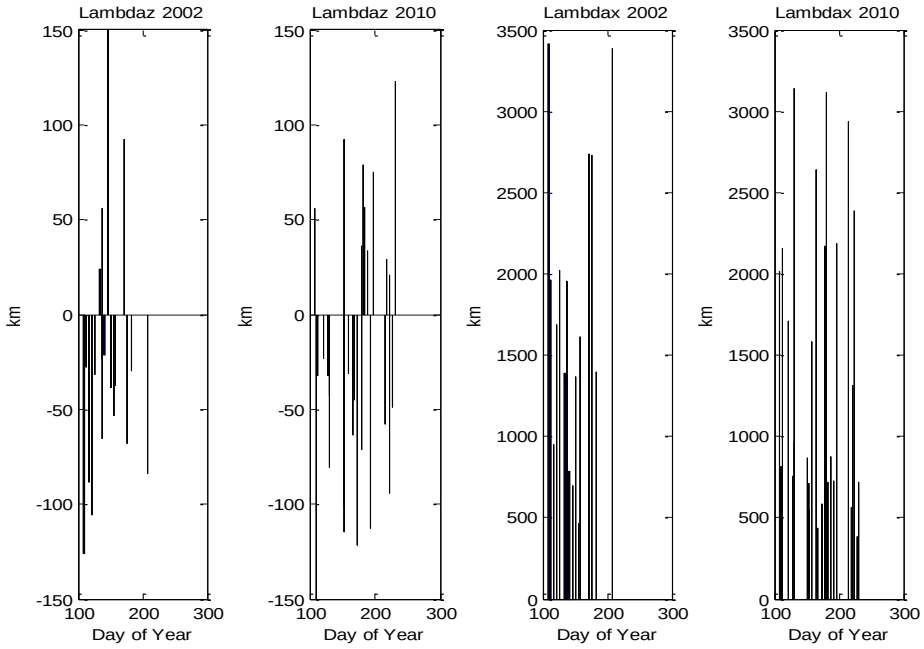

Figure 4-10: Wavelengths with winds included. Negative values indicate negative wavenumber

The magnitudes of the vertical phase speeds (Figure 4-11) in the 2010 season is on average higher than in the 2002 season which is due to the longer vertical wavelengths in 2010. The horizontal phase speeds however do not show the same variation as the vertical phase speeds because they have similar magnitudes between the seasons.

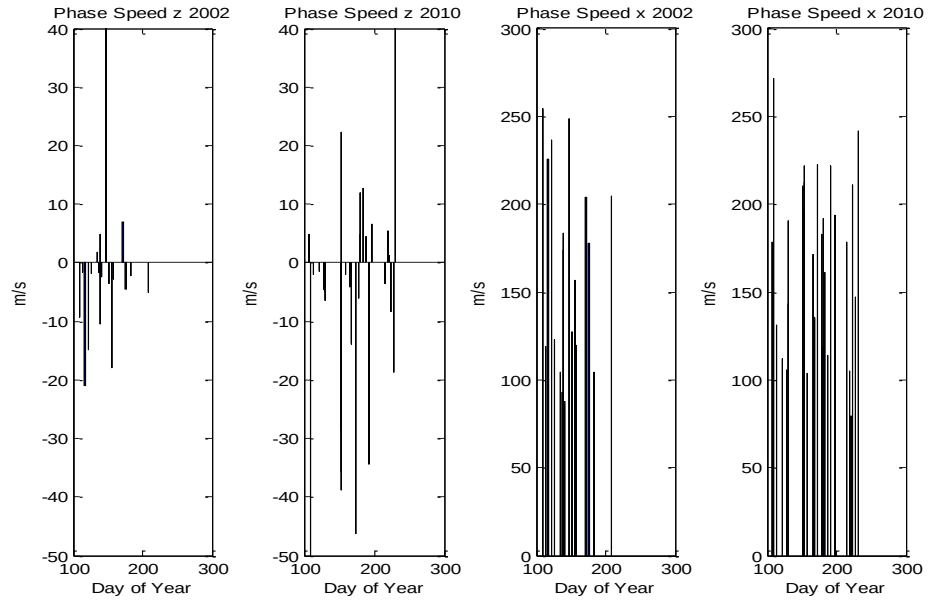

Figure 4-11: Phase Speeds with winds included. Negative values indicate negative wavenumber

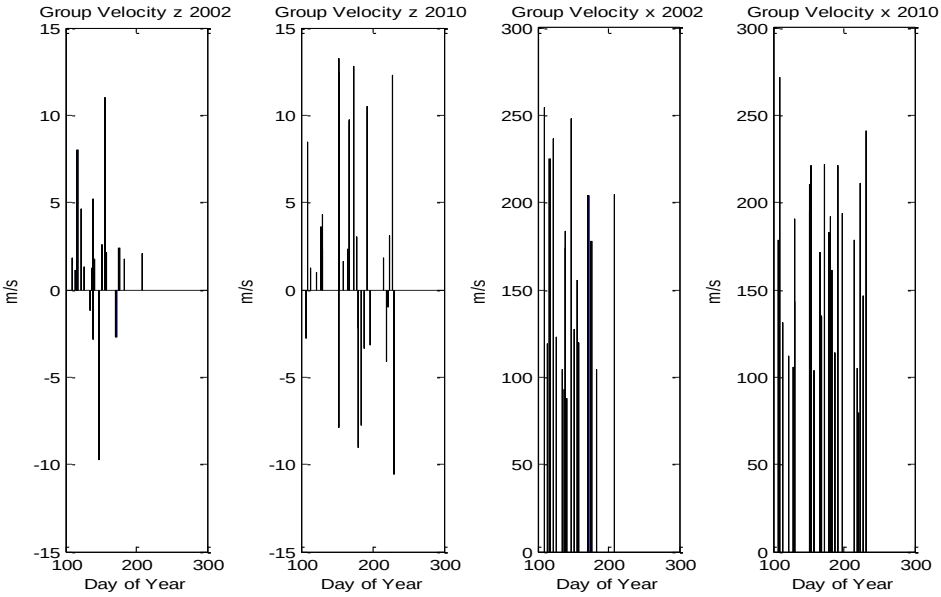

Figure 4-12: Group Velocities with winds included

The vertical group velocities, seen in Figure 4-12, for 2002 share similar magnitudes with the waves detected using the temperatures in both layers whereas the horizontal group velocities are larger on average for the 2010 season.

	2002	2010	Percent Difference from 2002 to 2010
Average detected period	187.5 minutes ±78.7	139.7 minutes ±93.7	-29% ±107%
Average λ_z	63.6 km±9.7	67.5 km±6.6	6% ±25%
Average λ_x	1,725 km±204.3	1,323 km±168.9	-26% ±24%
Average c_z	9.7 m/s±3.3	15.3 m/s±2.6	45% ±48%
Average c_x	163.5 m/s±13.2	168.6 m/s±9.04	3% ±13%
Average v_{gz}	3.5 m/s±0.71	6.1m/s±0.78	54% ±31%
Average v_{gx}	163.4 m/s±13.2	168.2 m/s±9.02	3% ±13%
% Propagating Upward	29%	52%	--

Table 3: Averages of all wave parameters using Brightness and Temperature in OH layer

Table 3 shows that all wave parameters except the average wave period and the average horizontal wavelengths increased from 2002 till 2010. The errors on the percent differences reveal that the average horizontal wavelengths, and the average vertical group velocities do not cross zero percent difference. Conversely, the average detected wave period, the average vertical wavelengths, the average vertical phase speed and the horizontal phase and group velocities percent differences may cross zero so are inconclusive.

4.4 USING BRIGHTNESS AND TEMPERATURE ONLY IN THE O_2 LAYER

The same method for deriving gravity wave parameters using the brightness and temperature of the OH layer are used for deriving these parameters using the brightness and temperature of the O_2 layer. These wave periods ranged from 25 minutes up to 4.5 hours. The vertical wavelengths in Figure 4-13 do have a noticeable increase in 2010 when compared to 2002. Unlike using the brightness and temperatures for the OH, both seasons showed a similar

number of waves with downward energy propagation. The horizontal wavelengths are very similar between seasons with 2010 having a few wavelengths exceeding 3500km.

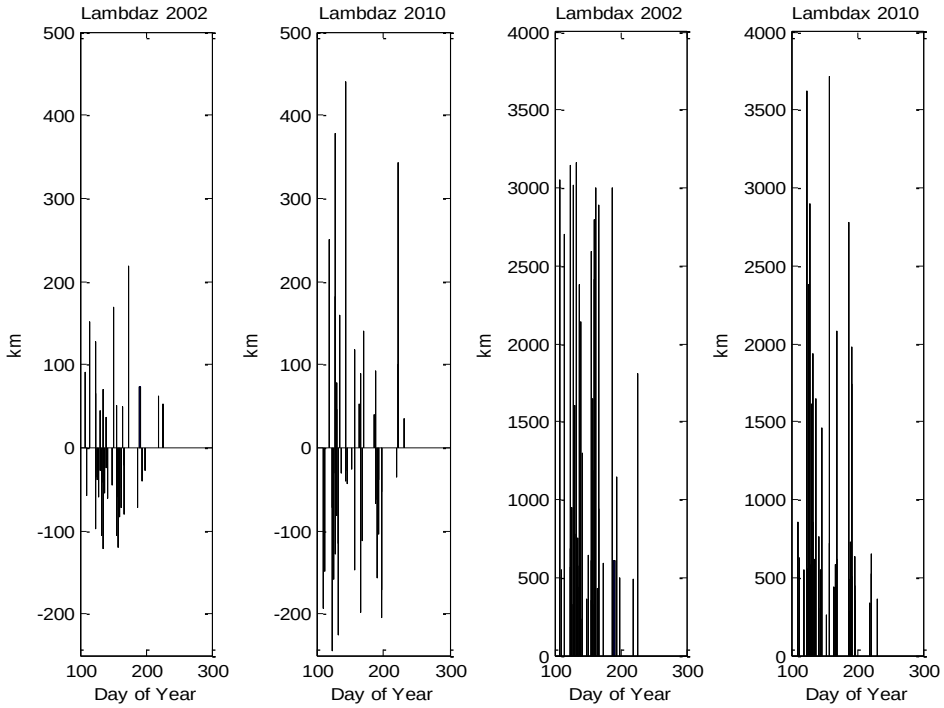

Figure 4-13: Wavelengths with winds included. Negative values indicate negative wavenumber

The vertical phase speeds and group velocities for 2010 in Figure 4-14 show the same increase in magnitude between the two seasons as seen in the wavelengths. Their magnitudes are also similar to the method using the brightness and temperature in the OH layer. Conversely, the horizontal components only show a slight increase of average magnitudes between seasons.

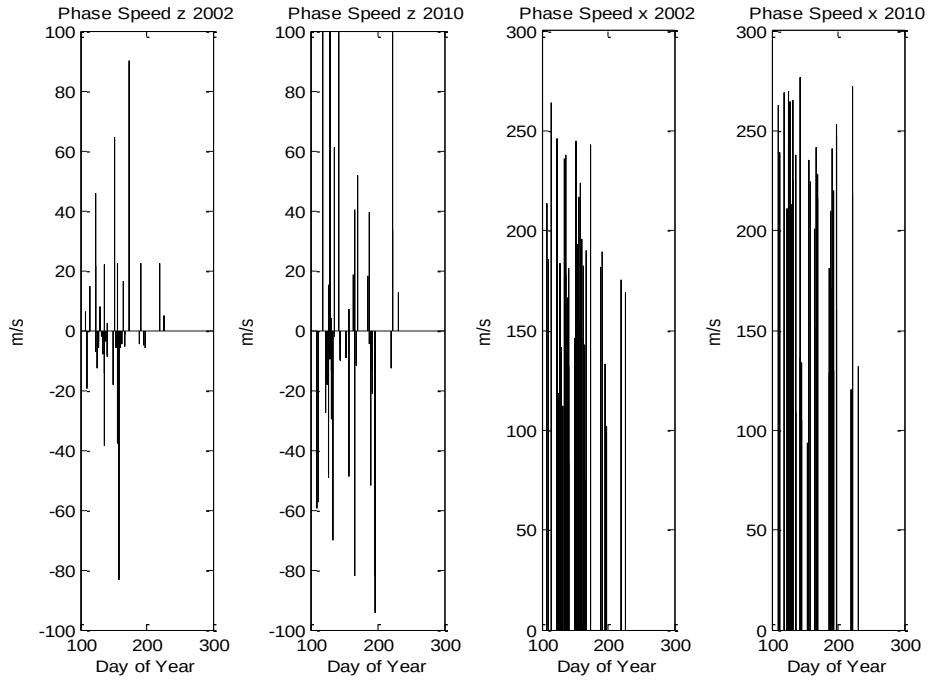

Figure 4-14: Phase Speeds with winds included. Negative values indicate negative wavenumber

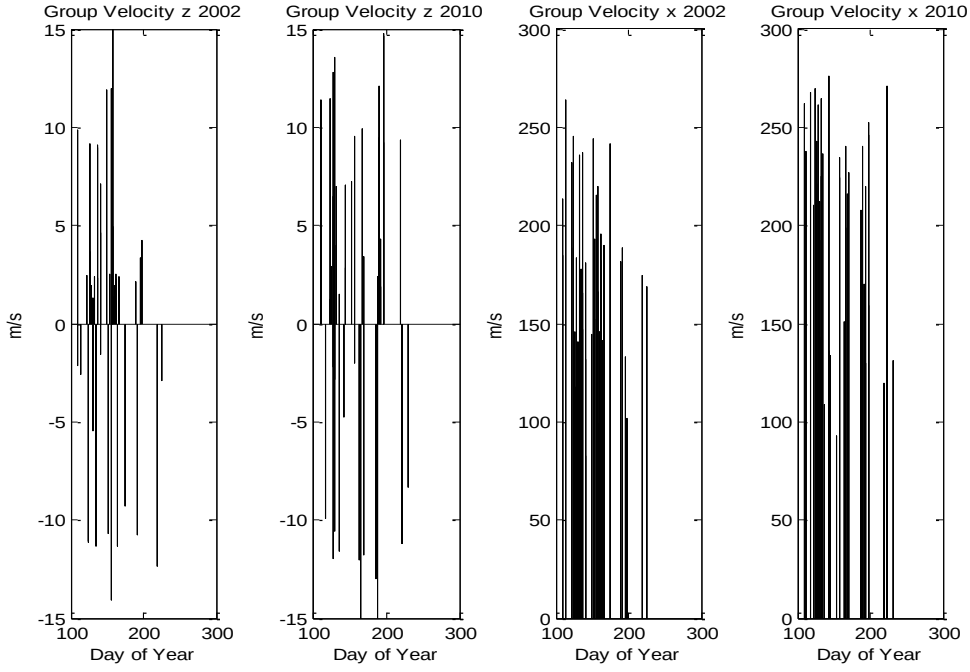

Figure 4-15: Group Velocities with winds included

Figure 4-15 shows the same patterns in the group velocities between the two season as exhibited in the wavelengths and phase speeds.

	2002	2010	Percent Difference from 2002 to 2010
Average detected period	136.6 minutes ±92.3	88.5 minutes ±77.8	-43% ±149%
Average λ_z	71.6 km±6.6	126.9 km±14.7	56% ±19%
Average λ_x	1,416 km±165	1,032 km±139	-31% ±25%
Average c_z	17.1 m/s±3.3	45.1 m/s±8.9	90% ±31%
Average c_x	174.0 m/s±7.5	201.5 m/s±8.3	15% ±8%
Average v_{gz}	6.4 m/s±0.78	8.3 m/s±0.66	26% ±20%
Average v_{gx}	173.5 m/s±7.4	200.8 m/s±8.3	15% ±8%
% Propagating downward	54%	59%	--

Table 4: Averages of all wave parameters using Brightness and Temperature in O_2 layer

Table 4 gives the averages in each season. All parameters except the detected wave period and horizontal wavelength increased from the 2002 season to the 2010 season. Only the average detected wave periods were within a standard deviation of each other. All other wave parameters between the 2002 season and the 2010 were more than one standard deviation away from each other.

4.5 COMPARING ALL WAVES

	2002	2010	Percent Difference from 2002 to 2010
Average detected period	146.2 minutes ±86.8	121.7 minutes ±91.7	-18% ±133%
Average λ_z	68.5km±4.2	85.2km±6.9	22% ±14%
Average λ_x	1,451km±94.6	1,223km±91.5	-17% ±14%

Average c_z	13.74m/s±1.6	24.6m/s±3.8	57% ±25%
Average c_x	167.1m/s±4.8	173.3m/s±5.3	3.6% ±6%
Average v_{gz}	5.4m/s±0.4	6.6m/s±0.4	20% ±%13
Average v_{gx}	166.7m/s±4.9	172.7m/s±5.3	3.5% ±%6
% Propagating downward	30%	31%	--

Table 5: All Waves Combined Property Averages

There were several overall differences in Table 5 that occurred between the 2002 and the 2010 seasons. Most of the wave parameter experienced an overall increase from 2002 till 2010 except for the horizontal wavelengths. Conversely, the horizontal phase speed and group velocity saw a modest increase. All of the average vertical components increased by at least 20%. The proportion of downward energy propagating waves to upward energy propagating waves remained very similar. Calculating the errors on the percent differences reveals that all of the vertical components differences do not cross zero in addition to the horizontal wavelength. The horizontal phase and group velocity and the average wave period exhibited errors that cross zero percent difference.

The larger vertical wavelengths for the 2010 season can easily be seen in Figure 4-16. The vertical wavelengths for the 2002 season were all less than 200km with a large number being within the -25km to -50 km range indicating negative wavenumbers. The waves with downward energy propagation were more spread out in their wavelengths. The 2010 season featured some similarities but had some waves with longer wavelengths which account for the increased average. The gaps around zero are due to the wavelength filtering for temperatures mentioned previously.

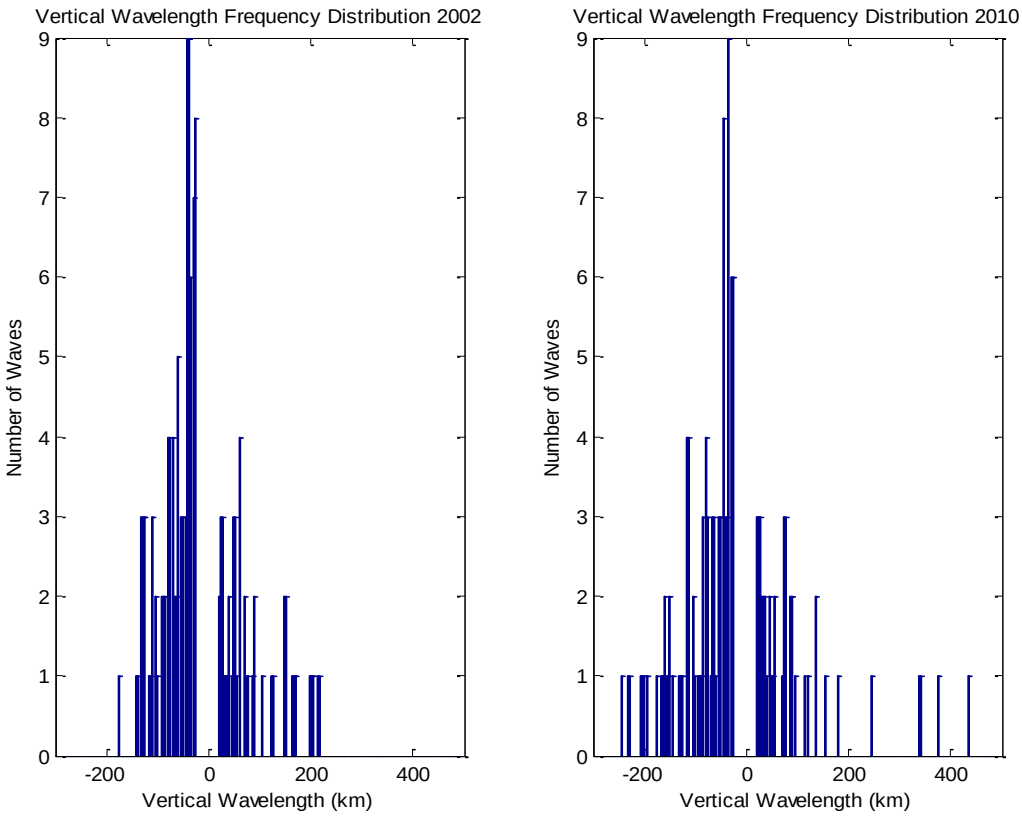

Figure 4-16: Gravity Wave Vertical Wavelength Frequency Distribution. Negative values indicate negative wavenumber

Since this thesis is about the solar cycle influence on gravity wave activity it would be worthwhile to compare the number of detected waves and the geomagnetic AP index. This index is a measure of the geomagnetic activity on the earth and is a 3 hour average from 13 monitoring stations around the earth [NOAA]. The frequency distribution in Figure 4-17 shows that most waves occurred during time at which the magnetic index is between 0 and 10 and falling off from there with a small spike in waves between AP index values of 15 and 20 in both years. This pattern is similar for both the 2002 and the 2010 season with the most waves detected in the 5-10 range for 2002 and 2010 having the most detected in the 0-5 range.

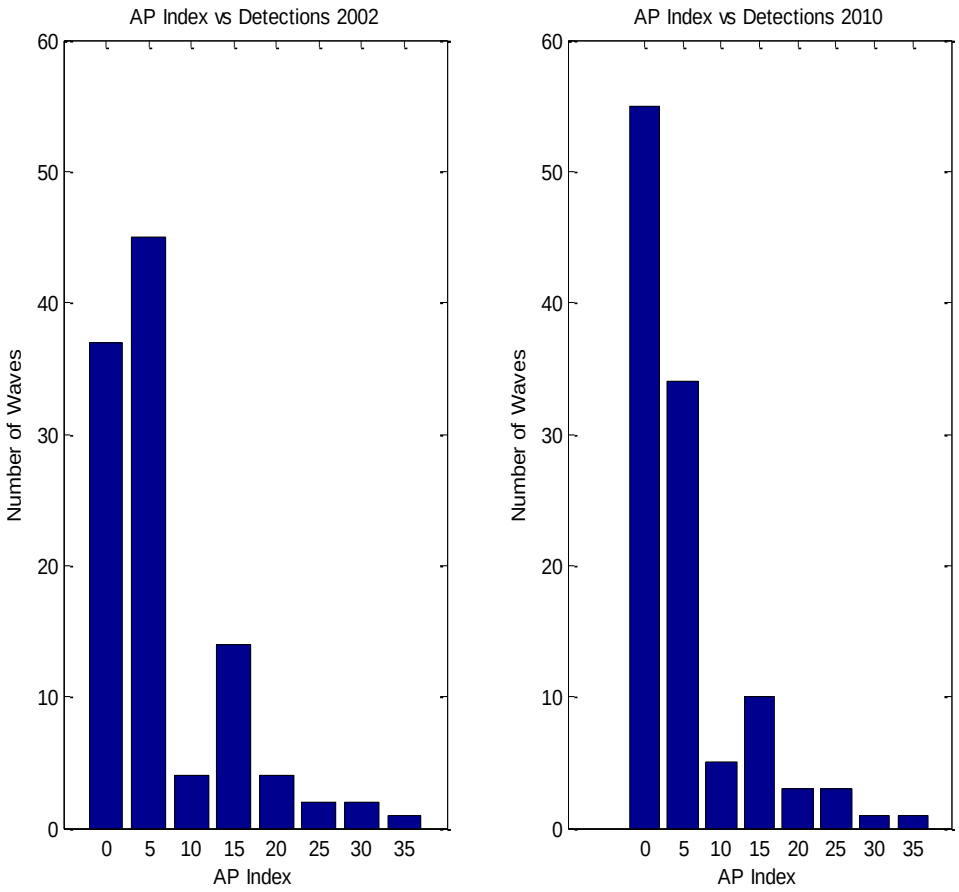

Figure 4-17: Gravity Wave Detection vs AP Index

Normalizing each AP index bin by the number of times that AP index occurred in the season gives Figure 4-18. The normalization decreases the weight of the low AP index bins because there were many recorded times of low AP index. As seen in the plot, the distributions are more even in 2002 with a slight tendency toward the higher bins for 2010. The overall normalized totals were also higher in 2010 even with a similar number of wave detections in both years.

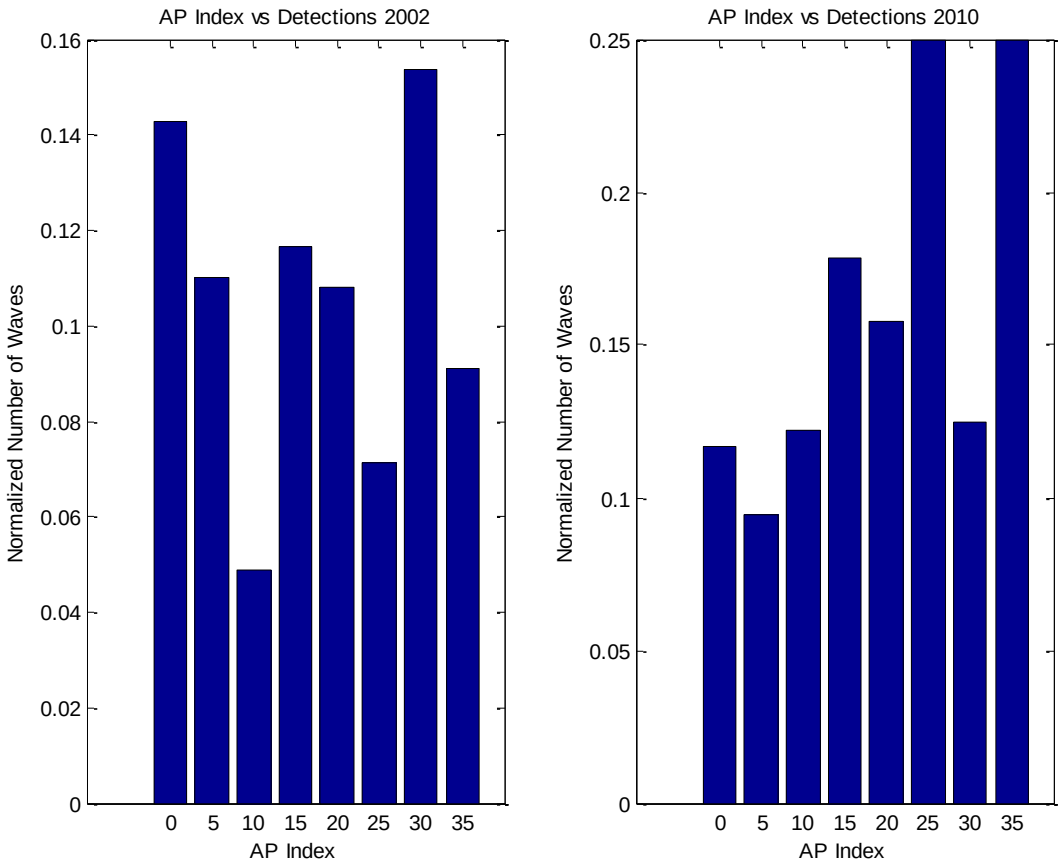

Figure 4-18: Normalized gravity wave detections vs AP index

Plotting all of the vertical wavelengths detected using all 4 methods yields the plot in Figure 4-189 (on the next page). The blue bars are the waves detected using the brightness in both layers, the red bars are the from the waves using temperature in both layers, the cyan bars are for waves using only the OH and the yellow bars are for waves using only the O_2 layer. As seen in the individual cases the waves using the O_2 layer featured some large vertical wavelength gravity waves compared to all of the other methods. The 2010 season also had waves that had larger vertical wavelengths. The 2002 season only had 3 waves larger than 200km whereas the 2010 season had 9 such waves. The 2010 season also had a more even distribution of waves across the season. More waves were detected in the first half of 2002 than the second half.

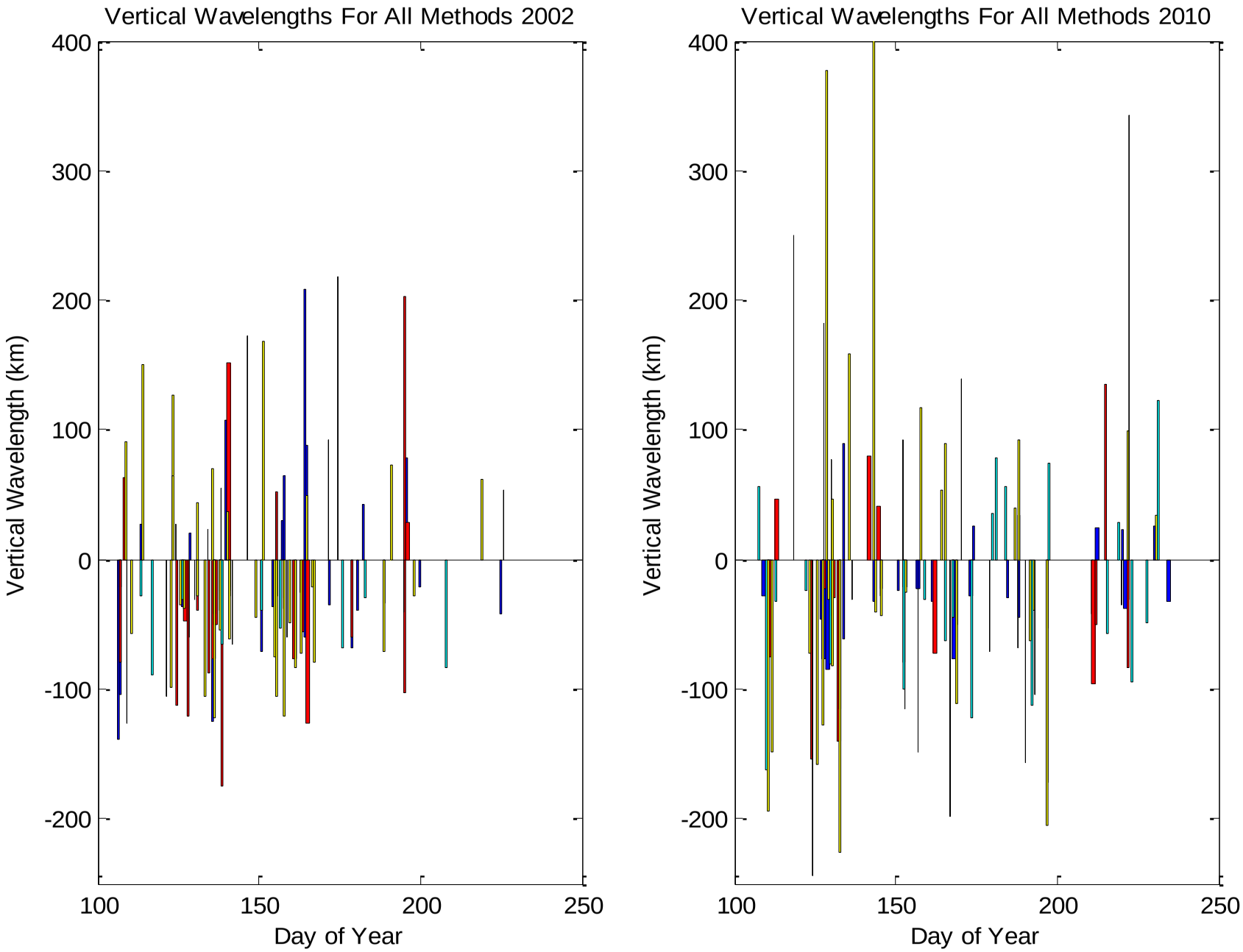

Figure 4-19: Vertical Wavelengths found with all methods. Negative values indicate negative wavenumber

4.6 COMPARISON WITH PREVIOUS RESULTS

Reisin and Scheer [1996, 2001] used the Tarasick and Hines theory for a single airglow layer to derive information about the vertical propagation of gravity waves for the OH(6-2) and O_2(0-1) airglow layers. The 1996 paper dealt with gravity waves with periods ranging from 3 hours to 24 hours for sporadic dates in 1986, 1987, 1992, and 1996, while the 2001 paper used the same method for waves with periods between 17 minutes and 2.8 hours continuously from 1997 till 2000. When plotting the complex Krassovsky ratio on the complex plane, shown in Figure 4-20, they found that for the waves in the tidal range nearly all fell within the fourth quadrant which corresponds to a positive real value of the ratio and a negative phase difference between the brightness and temperature fluctuations in both the OH and O_2 layers.

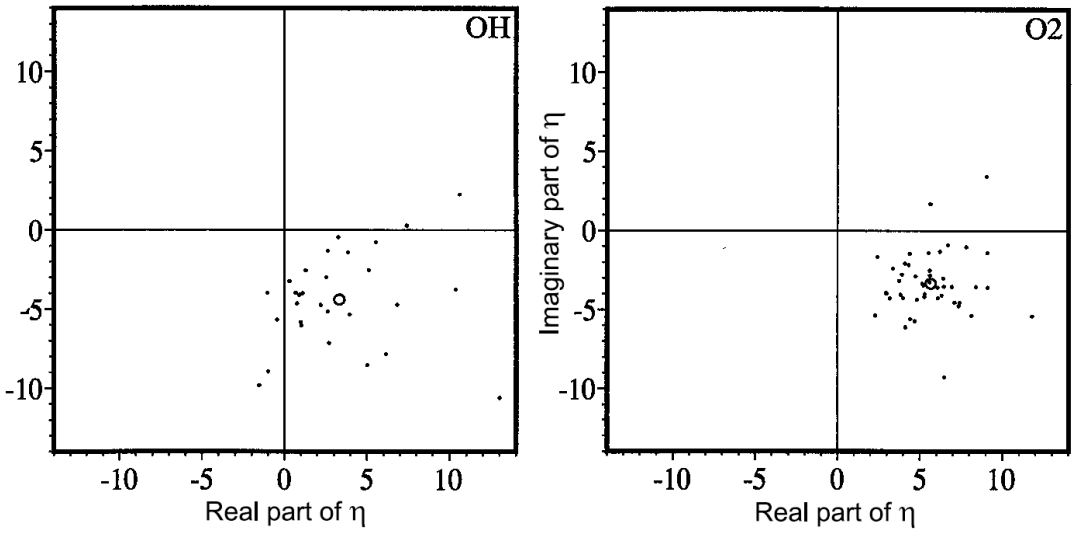

Figure 4-20: Krassovsky Ratio for tidal range gravity waves

[Reisin and Scheer, 1996]

When plotting the same in the 2001 paper for gravity waves between 17 minutes and 2.8 hours (Figure 4-21) they found that most of the waves had values in the first and fourth quadrants with a few in the second and third which indicates both upward and downward energy propagation.

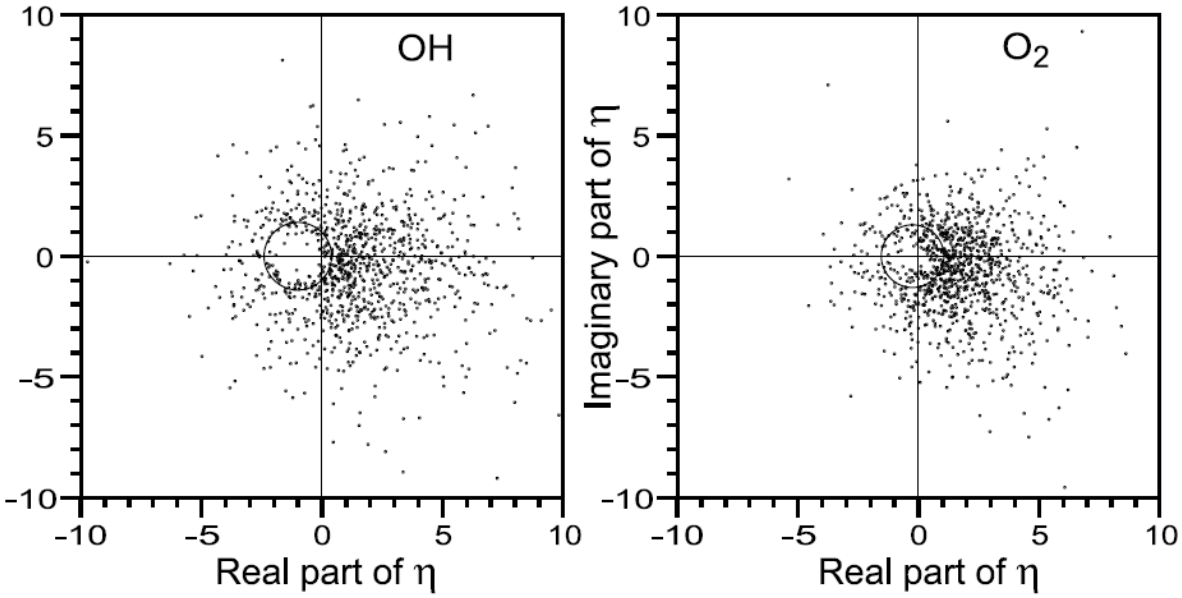

Figure 4-21: Krassovsky Ratio for shorter period gravity waves

[Reisin and Scheer, 2001]

Similar plots of the Krassovsky ration were created using the data presented here to check for consistency with previous results. Figure 4-22 shows the complex Krassovsky ratio for gravity waves detected in the OH airglow layer with Figure 4-23 showing the complex Krassovsky ratio for wave detected in the O_2 airglow layer.

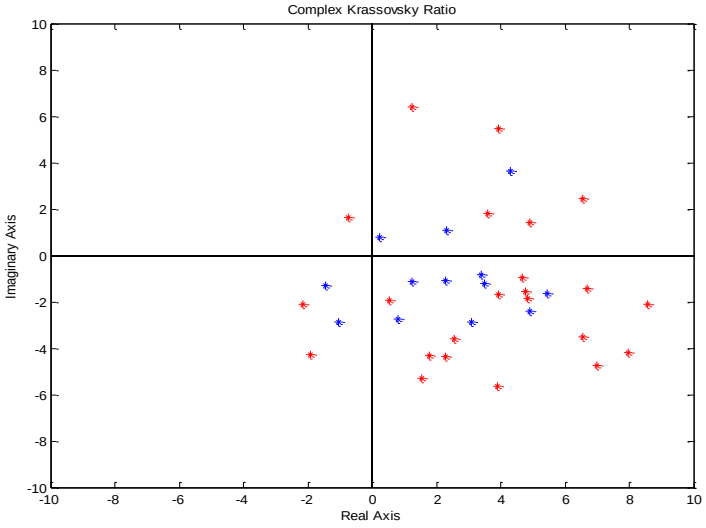

Figure 4-22: Complex Krassovsky Ratio for OH (2002 in red and 2010 in Blue)

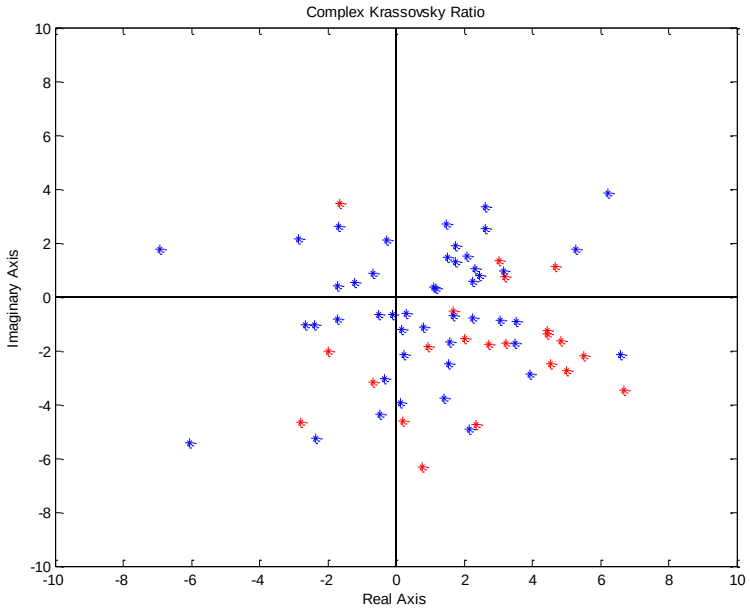

Figure 4-23: Complex Krassovsky Ratio for O_2 (2002 in red and 2010 in Blue)

The plots for both the OH and O_2 show several similarities to the Reisin and Scheer results. These results presented here show a slight tendency toward the fourth quadrant which was the case waves for with periods greater than 3 hours in Reisin and Scheer [1996]. The range chosen for this analysis are for waves between 5 minutes and 5 hours which overlaps slightly with the tidal range gravity waves seen in Figure 4-20. This overlap causes the slight tendency seen in Figure 4-22 and Figure 4-23.

There one difference between the Reisin and Scheer results and the presented results involves the percentage of downward propagating waves. For waves between 17 minutes and 2.8 hours, they found 39% of waves had downward energy propagation in the OH layer and 30% in the O_2 layer. The presented data in Table 6 for both seasons show that a greater percent of waves propagate downward in the O_2 layer compared to the OH layer.

	2002	2010	Reisin and Scheer
OH Layer	22%	34%	39%
O_2 Layer	35%	37%	30%

Table 6: Percentage of downward propagating waves compared to Reisin and Scheer [2001]

CHAPTER 5 - CONCLUSION

5.1 SUMMARY

Atmospheric gravity waves play an important role in the momentum and energy balance of the entire atmosphere by transporting this energy from the troposphere and stratosphere into the upper mesosphere and lower thermosphere. One of their most visible effects is in their breaking causing the cooler temperatures in the mesopause compared to the winter. Seasonal effects have been observed in gravity wave amplitudes and energy flux but solar cycle dependence has not been previously reported.

The solar cycle and its effect on the climate of the Earth is still not a well understood phenomenon. While the Maunder Minimum is an example of a global climate change occurring at the same time as an extended drop in solar activity, there is still some doubt as to whether this was a direct cause or a coincidence with some other large scale events combining together to cool the planet. A major difficulty in examining this relationship lies in the long data sets required to effectively draw conclusions over the entire 11 year cycle. It can be problematic to acquire an uninterrupted time series of temperatures or winds for such a long period of time due to unforeseen conditions such as instrument failure or a lack of sufficient funding. With more and more of these long data sets being recorded, analysis of solar cycle dependencies have been made possible such as the diurnal tide's change in intensity from solar maximum to solar minimum.

Using a modified Czerny-Turner grating spectrometer stationed at the Amundsen-Scott South Pole research station, temperature and brightness time series for the OH(6-2) airglow and the O_2(0-1) airglow have been analyzed for gravity wave signatures. The 2002 data gathering

season, during the last solar max, and the 2010 data gathering season, several months after solar minimum were used to observe variation in gravity wave parameters through the last solar cycle. A total of 110 gravity waves were detected in the 2002 season and 112 in the 2010 season. There was found to be an overall increase in several wave parameters from the 2002 season to the 2010 season for waves using four different detection methods. The largest change was in the vertical phase velocity and vertical wavelength. The horizontal wavelength however was found to have an average decrease from 2002 to 2010. When the errors on the percent differences were taken into account, all average vertical components in addition to the average horizontal wavelengths displayed differences that are greater than zero. The average wave period and the horizontal phase and group velocities had errors that caused the differences to cross zero so their differences are inconclusive.

The gravity wave detections found were compared with Reisin and Scheer for consistency. The magnitudes of the vertical components were found to be in agreement with the only difference being the amount of downward propagating waves in one layer compared to the other.

5.2 FUTURE WORK

This analysis only uses the 2002 and 2010 years so a more thorough analysis can be done by also investigating the intervening years so a trend in the gravity wave parameters can be found. The analysis method for the detection of gravity waves propagating in two separate airglow layers can be used on all of the CCD spectrometer data stored in the Embry-Riddle Space Physics Research Lab. This data spans the past two decades at various sites such as Sondrestrom, Greenland, the South Pole, and Longyearbyen, Norway. The gravity wave analysis

can also be directly compared to atmospheric tides during the same time frames and locations for further evidence of solar cycle modulations of atmospheric tides and gravity waves.

The current analysis uses dispersion relations to infer the horizontal properties of any detected gravity waves. Using a spectrometer in conjunction with another instrument such as an all-sky camera can directly give the horizontal properties of these waves. This will allow for a complete characterization to be done. Currently, Embry-Riddle does not have an instrument at the South Pole research station due to a lack of funding, but the university does have both a Fabry-Perot interferometer and a Michelson Interferometer looking into the Florida night sky. An all-sky camera is also scheduled to be set up in the near future. By having all of these instruments running simultaneously for the next several years, an analysis of the solar cycles influence on all three types of atmospheric waves can be done in a similar manner as presented here.

REFERENCES

Azeem S. M. I. and G. G. Sivjee, "Multiyear observations of tidal oscillations in OH M(3,1) Rotational temperatures at South Pole, Antarctica", *J. Geophys. Res.*, 114, A06312, doi:10.1029/2008JA013976. 2009

Beldon, C. L., and N. J. Mitchell , "Gravity wave–tidal interactions in the mesosphere and lower thermosphere over Rothera, Antarctica (68°S, 68°W)", *J. Geophys. Res.*, 115, D18101, doi:10.1029/2009JD013617. 2010

Chamberlain and Hunten, "Theory of planetary atmospheres, second edition", Orlando florida, Academic Press, 1987

Computing the Pearson Correlation Coefficient, 2003. <http://www.stat.wmich.edu/s216/book/node122.html>

Drob D. P., et al., "An empirical model of the Earth's horizontal wind fields: HWM07", *J. Geophys. Res.*, 113, A12304, doi:10.1029/2008JA013668. 2008

Eddy, John A. "The Maunder Minimum", *Science*, vol. 192, no. 4245, pp. 1189-1202, 1976

Hecht, J. H., and R. L. Walterscheid, "Observations of the OH Meinel (6,2) and O2 atmospheric (0,1) Nightglow emissions from Maui during the ALOHA-90 Campaign", *Geophys. Res. Lett.*, 18(7), 1341-1344. 1991

Hecht, J., R. Walterscheid, G. Sivjee, A. Christensen, and J. Pranke, "Observations of wave-Driven Fluctuations of OH Nightglow Emission from Sondre Stromfjord, Greenland", *J. Geophys. Res.*, 92(A6), 6091-6099. 1987

Hickey, M., G. Schubert, and R. Walterscheid, "Gravity Wave-Driven Fluctuations in the O2 atmospheric (0-1) Nightglow from an Extended, Dissipative Emission Region", *J. Geophys. Res.*, 98(A8), 13717-13729. 1993

Hickey, M., and R. Walterscheid, "A note on gravity wave-driven volume emission rate Weighted temperature perturbations inferred from O2 atmospheric and O I 5577 airglow observations", *J. Geophys. Res.*, 104(A3), 4279-4286. 1999

Hickey M. P. and Y. Yu, "A full-wave investigation of the use of a "cancellation factor" in gravity wave–OH airglow interaction studies", *J. Geophys. Res.*, 110, A01301, doi:10.1029/2003JA010372. 2005

Hines C. O., "Internal Atmospheric Gravity waves at Ionospheric Heights", *Can. J. Phys.* 38, 1960

Hines, C.O., and D.W. Tarasick, "On the detection and utilization of gravity waves in airglow studies", *Planet. Space Sci.* 35, 851-866, 1987

Krassovsky, V. I., "Infrasonic variation of OH emission in the upper atmosphere", *Ann. Geophys.*, 28, 739-746, 1972

Lindzen, R. S., "Turbulence and Stress Owing to Gravity Wave and Tidal Breakdown", *J. Geophys. Res.*, 86(C10), 9707-9714. 1981

Liu A. Z. and G. R. Swenson, "A modeling study of O_2 and OH airglow perturbations induced By atmospheric gravity waves", *J. Geophys. Res.*, 108, 4151, doi:10.1029/2002JD002474. 2003

Mutiso C., "Optical emissions generated during ionospheric heating", Master's Thesis, Embry-Riddle Aeronautical University, 2008

Nappo, Carmen J. *An Introduction to Atmospheric Gravity Waves*. San Diego, California: Academic Press, 2002.

NOAA, "Geomagnetic kp and ap indices", 2011. <http://www.ngdc.noaa.gov/stp/geomag/kp_ap.html>

Oznovich, I., D. J. McEwen, and G. G. Sivjee, "Temperature and airglow brightness oscillations in the polar mesosphere and lower Thermosphere", *Planet. Space Sci*, 43, 1121-1130, 1995

Patel, Azeem, "Observations of 6-hour and 8-hour period waves at the south pole", Poster, 2010

Picone J. M., A.E. Hedin, D.P. Drob, and A.C. Aikin, "NRL-MSISE-00 Empirical Model of the Atmosphere: Statistical Comparisons and Scientific Issues," *J. Geophys. Res.*, doi:10.1029/2002JA009430, 2003

Rauthe, Gerding, and Lubken, "Seasonal Changes in gravity wave activity measured by lidars at mid-latitudes", *Atmos. Chem. Phys. Discuss.*, 8, 13741-13773. 2008

Reisin, E., and J. Scheer, "Characteristics of atmospheric waves in the tidal period range derived from zenith observations of O2(0–1) Atmospheric and OH(6-2) airglow at lower midlatitudes", *J. Geophys. Res.*, 101(D16), 21223-21232. 1996

Reisin, E., and J. Scheer, "Vertical Propagation of Gravity Waves Determined from Zenith Observations of Airglow", *Advances in Space Research*, 27(10), 1743-1748, 2001

Savitzky-Golay,2010. <http://www.statistics4u.info/fundstat_eng/cc_filter_savgolay.html>

Scargle, J.D., "Studies in astronomical time series analysis. II - Statistical aspects of spectral analysis of unevenly spaced data*", Astrophysical Journal, Part 1*, Vol. 263, Dec. 15, 1982, p.835-853. 1982

Schlapp, R. "Fine struction in the $X^3\Sigma_g$- ground states of the oxygen molecule, and the rotational intensity distribution in the atmospheric oxygen band", *Phys. Rev.*, 51, 341, 1937.

Shunk , R. W., Mathematical structure of transport equations for multispecies flows, *Rev. Geophys., 15*(4), 429–445, doi:10.1029/RG015i004p00429. 1977

Simkhada D. B., J. B. Snively, M. J. Taylor, and S. J. Franke, "Analysis and modeling of ducted and evanescent gravity waves observed in the Hawaiian airglow", *Ann. Geophys.*, 27, 3213-3224, 2009

Sivjee, G., and R. Hamwey , "Temperature and Chemistry of the Polar Mesopause OH", *J. Geophys. Res.*, 92(A5), 4663-4672. 1987

Sivjee, G., D. Shen, J.-H. Yee, and G. Romick, "Variations, with peak emission altitude, in auroral O2 atmospheric (1, 1)/(0, 1) ratio and its relation to other auroral emissions", *J. Geophys. Res.*, 104(A12), 28003-28018. 1999

Sivjee, G., R. Walterscheid, J. Hecht, R. Hamwey, G. Schubert, and A. Christensen, "Effects of Atmospheric Disturbances on Polar Mesopause Airglow OH Emissions", *J. Geophys. Res.*, 92(A7), 7651-7656. 1987

Swenson, G., S. Mende, and S. Geller, "Fabry-Perot Imaging Observations of OH(8-3): Rotational Temperatures and Gravity Waves", *J. Geophys. Res.*, 95(A8), 12251-12263. 1990

Tarasick, D.W., and C.O. Hines, "The observable effects of gravity waves in airglow emissions", *Planet. Space Sci.* 38, 1105-1119, 1990

Weisstein, Eric W. "Hanning Function." From *MathWorld*--A Wolfram Web Resource. http://mathworld.wolfram.com/HanningFunction.html

Wittke, http://www4.nau.edu/microanalysis/microprobe-sem/statistics.html

Yee, J.-H., R. Niciejewski, and M. Z. Luo, "Observations of O2 ($^1\Sigma$) and OH nightglow during the ALOHA-90 Campaign", *Geophys. Res. Lett.*, 18(7), 1357-1360. 1991

Zhang, S .P., R. N. Peterson, R. H. Wiens and G. G. Shepherd, "Gravity Waves from O_2 Nightglow during the AIDA '89 campaign, I, Emission rate/temperature observations", *J. Atmos. Terr. Phys.*, 55, 355-375, 1993a